

# REVEALING THE MILKY WAY'S HIDDEN CIRCUMGALACTIC MEDIUM WITH THE COSMIC ORIGINS SPECTROGRAPH QUASAR DATABASE FOR GALACTIC ABSORPTION LINES

Y. ZHENG<sup>1,2,3</sup>, J. E. G. PEEK<sup>4,5</sup>, M. E. PUTMAN<sup>3</sup>, AND J. K. WERK<sup>6</sup>

<sup>1</sup> Department of Astronomy, University of California, Berkeley, CA 94720, USA; yongzheng@berkeley.edu

<sup>2</sup> Miller Institute for Basic Research in Science, University of California, Berkeley, CA 94720, USA

<sup>3</sup> Department of Astronomy, Columbia University, New York, NY 10027, USA

<sup>4</sup> Space Telescope Science Institute, 3700 San Martin Dr, Baltimore, MD 21218, USA

<sup>5</sup> Department of Physics & Astronomy, Johns Hopkins University, Baltimore, MD 21218, USA

<sup>6</sup> Department of Astronomy, University of Washington, Seattle, WA 98195-1580, USA

## ABSTRACT

Every quasar (quasi-stellar object; QSO) spectrum contains absorption-line signatures from the interstellar medium, disk-halo interface, and circumgalactic medium (CGM) of the Milky Way (MW). We analyze *Hubble Space Telescope*/Cosmic Origins Spectrograph (COS) spectra of 132 QSOs to study the significance and origin of Si IV absorption at  $|v_{\text{LSR}}| \leq 100 \text{ km s}^{-1}$  in the Galactic halo. The gas in the north predominantly falls in at  $-50 \lesssim v_{\text{LSR}} \lesssim 0 \text{ km s}^{-1}$ , whereas in the south, no such pattern is observed. The Si IV column density has an average and a standard deviation of  $\langle N_{\text{SiIV}} \rangle = (3.8 \pm 1.4) \times 10^{13} \text{ cm}^{-2}$ . At  $|b| \gtrsim 30^\circ$ ,  $N_{\text{SiIV}}$  does not significantly correlate with  $b$ , which cannot be explained by a commonly adopted flat-slab geometry. We propose a two-component model to reconstruct the  $N_{\text{SiIV}} - b$  distribution: a plane-parallel component  $N_{\text{DH}}^\perp$  to account for the MW's disk-halo interface and a global component  $N_{\text{G}}$  to reproduce the weak dependence on  $b$ . We find  $N_{\text{DH}}^\perp = 1.3^{+4.7}_{-0.7} \times 10^{12} \text{ cm}^{-2}$  and  $N_{\text{G}} = (3.4 \pm 0.3) \times 10^{13} \text{ cm}^{-2}$  on the basis of Bayesian analyses and block bootstrapping. The global component is most likely to have a Galactic origin, although its exact location is uncertain. If it were associated with the MW's CGM, we would find  $M_{\text{gas,all}} \gtrsim 4.7 \times 10^9 M_\odot (\frac{C_f}{1}) (\frac{R}{75 \text{ kpc}})^2 (\frac{f_{\text{SiIV}}}{0.3})^{-1} (\frac{Z}{0.3 Z_\odot})^{-1}$  for the cool gas at all velocities in the Galactic halo. Our analyses show that there is likely a considerable amount of gas at  $|v_{\text{LSR}}| \leq 100 \text{ km s}^{-1}$  hidden in the MW's CGM. Along with this work, we make our QSO dataset publicly available as the COS Quasar Database for Galactic Absorption Lines (COS-GAL).

*Keywords:* Galaxy: halo - Galaxy: structure - quasars: absorption lines - techniques: spectroscopic

## 1. INTRODUCTION

The  $\Lambda$ CDM cosmology predicts that 16%<sup>1</sup> of the matter masses are in the form of baryons; however, observations of the low-redshift universe have so far found a limited amount of baryons. For example, Behroozi et al. (2010) suggested that only  $\sim 10 - 20\%$  of the predicted baryons are locked in stars for galaxies at  $z < 4$ . Peebles & Shankar (2011) found that, for  $L^*$  galaxies, only  $\sim 5\%$  of the predicted baryonic mass is in cold gas form (i.e., H I and H<sub>2</sub>). The baryon deficit is even more severe over intergalactic scales, where less than 10% of the predicted baryons exist in collapsed forms of stars in galaxies and hot gas in groups and clusters (Persic & Salucci 1992; Fukugita et al. 1998; Cen & Ostriker 1999; Bregman & Lloyd-Davies 2007; Shull 2014). Recent years have seen emerging evidence suggesting that galaxies are embedded

in massive multiphase plasma, the so-called circumgalactic medium (CGM). The existence of the CGM helps to alleviate the missing baryon problem because, generally speaking,  $\sim 10^9 - 10^{11} M_\odot$  of baryonic mass is estimated in the CGM for sub- to super- $L^*$  galaxies at  $z \lesssim 0.5$  (Tumlinson et al. 2013; Werk et al. 2013, 2014; Stocke et al. 2013; Liang & Chen 2014; Lehner et al. 2015; Burchett et al. 2016; Stern et al. 2016; Prochaska et al. 2017; Keeney et al. 2017; Bordoloi et al. 2018; Zahedy et al. 2018).

One of the tools proven most useful for studying the CGM of galaxies is absorption-line observations toward background quasars (quasi-stellar objects; QSOs), providing rest-frame observations of multiphase CGM with weakly (e.g., Mg II, Si II) or highly (e.g., Si IV, O VI) ionized metals. With statistically significant samples of QSO sightlines probing the CGM at various impact parameters, it has been found that dense gas is preferentially located at smaller impact parameters (e.g., Werk

<sup>1</sup>  $\Omega_b/\Omega_m = 16\%$ ,  $\Omega_b = 0.0486$ ,  $\Omega_m = 0.308$ ; Planck Collaboration et al. 2016.

et al. 2013; Lehner et al. 2015; Keeney et al. 2017). In particular, Werk et al. (2014) suggested a power-law form of the metal surface density of the CGM as  $N_{\text{Si}} \sim R^{-0.8} \text{ cm}^{-2}$ . For star-forming galaxies, Werk et al. (2013) found that the covering fraction of Si III and Si IV reaches  $\sim 95\%$  within 75 kpc of host galaxies, but the value drops to  $\sim 65\%$  at  $75 \leq R \leq 160$  kpc.

Inferred from the ubiquitous detection of CGM in extragalactic studies, our own Milky Way (MW) is most likely surrounded by a similar halo with abundant gas at various phases. The latest study of high-velocity gas in the MW halo using 270 QSO sightlines (Richter 2017) showed that  $77\% \pm 6\%$  of the Galactic sky is covered by warm-ionized gas (e.g., Si II, Si III, C II, C IV) moving at  $|v_{\text{LSR}}| = 100 - 500 \text{ km s}^{-1}$ . They estimated that the high-velocity gas contributes  $\sim 3 \times 10^9 M_{\odot}$  baryonic mass to the MW halo, 90% of which comes from the Magellanic Stream (Fox et al. 2014). The adopted high-velocity range is to avoid contamination of gas inside or near the Galactic disk; because as we sit inside the Galactic disk, every QSO spectrum unavoidably contains absorption-line signatures from the MW’s interstellar medium (ISM), disk-halo interface, and the CGM. Therefore, velocity is often used as a proxy for distance: gas with  $|v_{\text{LSR}}| \gtrsim 100 \text{ km s}^{-1}$  is selected to study those neutral/ionized high-velocity clouds at  $\sim 10 - 15$  kpc in the inner Galactic halo (e.g., Sembach et al. 2003; van Woerden et al. 2004; Wakker 2004; Shull et al. 2009; Lehner et al. 2012; Fox et al. 2014), whereas gas moving at  $|v_{\text{LSR}}| \lesssim 100 \text{ km s}^{-1}$  is typically deemed more nearby (see below). Hereafter we refer to the velocity range of  $|v_{\text{LSR}}| \lesssim 100 \text{ km s}^{-1}$  as the *low-intermediate* velocity gas, and refer to the range of  $|v_{\text{LSR}}| \gtrsim 100 \text{ km s}^{-1}$  as the *high-velocity* gas.

The low-intermediate velocity gas in the MW is studied using halo star sightlines and background QSO sightlines in the context of the disk-halo interface, which is modeled as a plane-parallel flat slab with a scale height of a few kiloparsecs above the Galactic plane (e.g., Savage et al. 2003; Savage & Wakker 2009; Wakker et al. 2012). However, extragalactic CGM studies have shown that most ionic absorbers at a wide range of impact parameters are found to be gravitationally bound with centroid velocities of  $|\delta_v| \lesssim 200 \text{ km s}^{-1}$  from host galaxies’ systemic velocities (Werk et al. 2013; Keeney et al. 2017). In addition, Zheng et al. (2015) pointed out that the MW’s extended CGM is likely to host a similar amount of gas moving at both high and low-intermediate velocities, regardless of the gas phase, by making synthetic observations of a simulated MW-mass galaxy halo (Joung et al. 2012).

Here we leverage the *Hubble Space Telescope* Spectroscopic Legacy Archive (HSLA; Peebles et al. 2017) to revisit the ion distribution at low-intermediate velocities in the MW’s disk-halo interface and CGM. Ions such as

C II, Si II, and Si III, are so strong that they are often fully saturated and can only be used to study the gas at  $|v_{\text{LSR}}| > 100 \text{ km s}^{-1}$ . For gas moving at  $|v_{\text{LSR}}| \leq 100 \text{ km s}^{-1}$ , usually transition lines at high-ionization stages are preferred, such as Al III, Si IV, C IV, and O VI (e.g., Savage et al. 2003; Savage & Wakker 2009; Wakker et al. 2012). In this work, we focus on the Si IV doublet at 1393/1402 Å to study the warm-ionized gas at  $|v_{\text{LSR}}| \leq 100 \text{ km s}^{-1}$  over the Galactic sky at  $|b| \gtrsim 30^{\circ}$ .

The article is organized as follows: § 2 introduces our data reduction of the *HST*/Cosmic Origins Spectrograph (COS) spectra, including continuum fitting, column-density and centroid-velocity calculations, and evaluation of line saturation. We make our continuum-normalized spectra publicly available as described in § 2.1. In § 2.2, we describe additional data reduction for the Si IV  $\lambda 1393/1402\text{\AA}$  doublet, which will be the focus of later analyses. In § 3 we study the all-sky distribution of the low-intermediate Si IV absorbers. We compare our QSO measurements with a commonly adopted flat-slab model in § 4.1, and propose a new two-component model in § 4.2. In § 5, we discuss the caveats of the flat-slab model and our model (§ 5.1), investigate the origin of the global component (§ 5.2), and conduct an order-of-magnitude mass estimate for the global component in the context of the MW’s CGM (§ 5.3). We conclude in § 6.

## 2. DATA

### 2.1. General Data Overview

We obtain our QSO spectra from HSLA (Peebles et al. 2017). The first release of HSLA (February 2017) delivers uniformly reduced and coadded *HST*/COS spectra with M-mode (medium-resolution/ G130M and G160M) and L-mode (low-resolution/ G140L) observations. For each target, the spectra from different programs, epochs, and gratings are coadded to improve the signal-to-noise ratio (S/N) and the wavelength coverage. Three community codes are considered for spectral coaddition: (1) *coadd\_x2d* (Danforth et al. 2010; Keeney et al. 2012), (2) *coscombine* (Wakker et al. 2015), and (3) *counts\_coadd* (Tumlinson et al. 2013). HSLA adopted the in-common steps among these codes: multiepoch spectra are shifted to the same wavelength grid by aligning strong interstellar lines that appear in every spectrum, and the wavelength grid is based on the values solved by the standard *calcos* pipeline. For the final products, HSLA arranges targets into different categories, such as *Solar System and Exoplanets*, *Stars and Galaxies and Clusters*. Detailed steps of spectral coaddition and target categories can be found in the HSLA document<sup>2</sup> (Peebles et al. 2017). In this work, we focus on the *QSOs*, *AGNs*, and *Seyferts* categories, which we will henceforth refer to as

<sup>2</sup> [http://www.stsci.edu/hst/cos/documents/isrs/ISR2017\\_04.pdf](http://www.stsci.edu/hst/cos/documents/isrs/ISR2017_04.pdf)

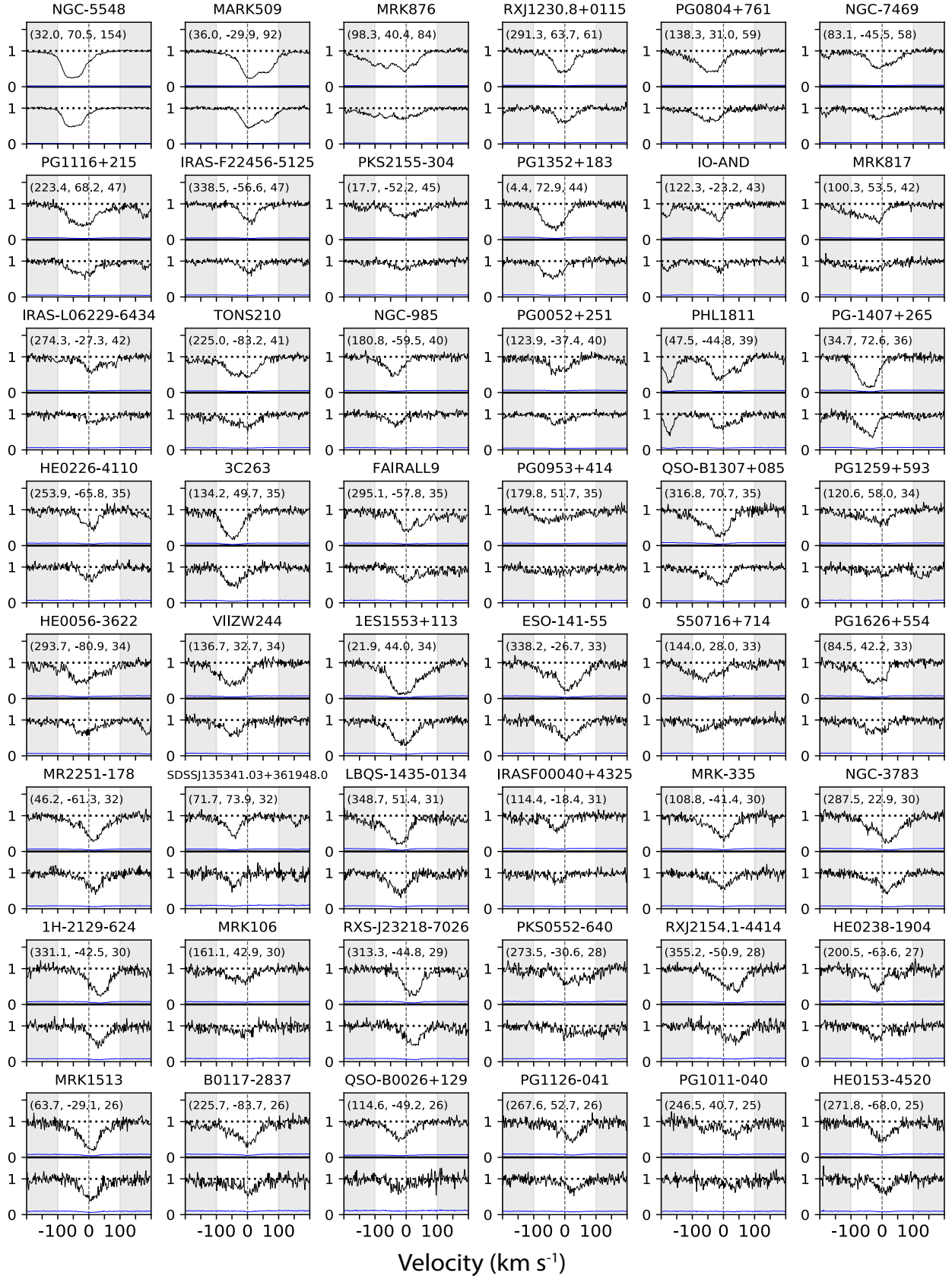


**Figure 1:** Continuum-normalized flux (black) and error (blue) of the Si IV doublet for the 119 spectrally non-saturated QSOs ( $Q=0$ ; see § 2.2). Spectra are shown in original resolution. For each target, we show the Si IV 1393/1402 lines in upper/lower panels, respectively, and the numbers in parenthesis indicate  $l$ ,  $b$ , and S/N per resolution element. Our analyses focus on the spectral region within  $|v_{\text{LSR}}| \leq 100 \text{ km s}^{-1}$ , as indicated in white shades.

the HSLA QSO catalog.

For M-mode observations, the HSLA QSO catalog includes coadded spectra of 467 QSOs with G130M grating and 305 QSOs with G160M grating. In total, there are 511 QSOs, among which 261 QSOs were observed with both G130M and G160M. HSLA characterizes each coadded spectrum with an average S/N, defined as the mean of the S/N values per resolution element<sup>3</sup> calculated over ten Å windows every 1000 Å starting from 1150 Å (Peeples et al. 2017). Our analyses focus on those QSOs with  $S/N \geq 5$ , which includes 385 (246) QSOs with G130M (G160M) grating. In total, there are 401 QSOs, among which 230 QSOs have both G130M and G160M observations. For these 401 QSOs, we perform continuum normalization for a series of interstellar absorption lines and focus on the spectral region within  $\pm 1000$  km s<sup>-1</sup> of the rest wavelength of each line. We use Linetools<sup>4</sup> package (Prochaska et al. 2016) to conduct continuum normalization, which is an in-development open-source one-dimensional spectral analysis package. Its continuum normalization function<sup>5</sup> makes use of an Akima Spline to generate the continua from absorption-free regions near the lines of interest. An interactive interface is generated for each spectrum, and we visually inspect the suggested continua and make local correction to account for higher-order continuum variation if needed.

We compile the continuum-normalized interstellar line spectra for the 401 QSOs into a full dataset as the COS Quasar Database for Galactic Absorption Lines (COS-GAL). For each target, COS-GAL includes the normalized spectra of a number of interstellar lines, including Fe II  $\lambda 1142/1143/1144/1608$  Å, P II  $\lambda 1152$  Å, S II  $\lambda 1250/1253/1259$  Å, C II  $\lambda 1334$  Å, C IV  $\lambda 1548/1550$  Å, Si II  $\lambda 1190/1193/1260/1526$  Å, Si III  $\lambda 1206$  Å, and Si IV  $\lambda 1393/1402$  Å. We note that the continuum-normalized spectra provided in COS-GAL are specifically processed to study the absorption lines associated with the ionized gas of the MW. We do not conduct detailed analyses on higher-redshift intervening absorbers along the line of sight (LOS); users should exercise caution when inspecting these spectra for potential line contamination. In addition, the COS-GAL spectral lines are not ideal for studies of any broad features intrinsic to host QSOs. Users interested in these features should examine the original spectra instead.

In addition to the ion lines, COS-GAL also includes H I 21cm emission lines extracted at the position of each QSO. We retrieve the H I spectra from three H I surveys at their native angular resolutions: GALFA-H I (4'; Peek

et al. 2018), HI4PI (16.2'; HI4PI Collaboration et al. 2016), and LAB (36'; Kalberla et al. 2005). We refer the reader to table 1 in HI4PI Collaboration et al. (2016) for a comparison of the three surveys. Note that the COS spectra are observed with an aperture size of only 2.5'', which is much smaller than the radio beam sizes. Thus, we caution that the ionized gas studied by COS-GAL and the neutral gas extracted from these H I surveys may not be entirely cospatial. We provide the H I spectra at various resolutions to partially investigate this and refer the reader to a study by Wakker et al. (2001) that examines the influence of different radio beam sizes on studies of high- and low-intermediate velocity clouds.

The COS-GAL dataset is made publicly available at [10.17909/T9N677]. In the following sections, we focus on the Si IV doublet  $\lambda 1393/1402$  Å to study the warm-ionized gas moving at low-intermediate velocity in the MW.

## 2.2. Data Reduction Focused on The Si IV Doublet

The Si IV doublet is covered by G130M grating, and the COS-GAL dataset provides 385 QSOs in this grating with mean  $S/N \geq 5$ . We examine the continuum-normalized Si IV doublet for each QSO and discard 95 targets that are with either unmatched absorption components or very poor spectral quality. For the remaining 290 QSOs with reliable Si IV absorption lines, we recalculate the S/N for the absorption-free continuum region between 1394 Å and 1401 Å and select 132 high-quality QSO spectra with S/N per resolution  $\geq 12$ . The Si IV doublets of these 132 QSOs form the core sample of our following analyses.

Because the COS pipeline and HSLA adopt a heliocentric frame in their products, here we correct the spectral velocity to the LSR frame:

$$v_{\text{LSR}} = v_{\text{hel}} + 9\cos(l)\cos(b) + 12\sin(l)\cos(b) + 7\sin(b) \quad (1)$$

and present the continuum-normalized Si IV doublets in Figures 1 and 2. Separately, Figure 1 shows the spectra of 119 QSOs classified as spectrally resolved ( $Q = 0$ ), whereas Figure 2 includes 11 QSOs with unresolved saturation ( $Q = 1$ ) and two with uncertain contamination ( $Q = -1$ ). The judgment of line saturation and the  $Q$  value is based on apparent column-density measurements, as described next.

To calculate the apparent Si IV column densities, we adopt the apparent optical depth (AOD) method (Savage

<sup>3</sup> G130M grating has six pixels per resolution (see the COS Data Handbook, Version 4, Rafelski & et al. 2018), therefore,  $S/N$  per resolution  $\equiv S/N$  per pixel  $\times \sqrt{6}$ .

<sup>4</sup> <https://github.com/linetools/linetools>

<sup>5</sup> <http://linetools.readthedocs.io/en/latest/xspectrum1d.html>

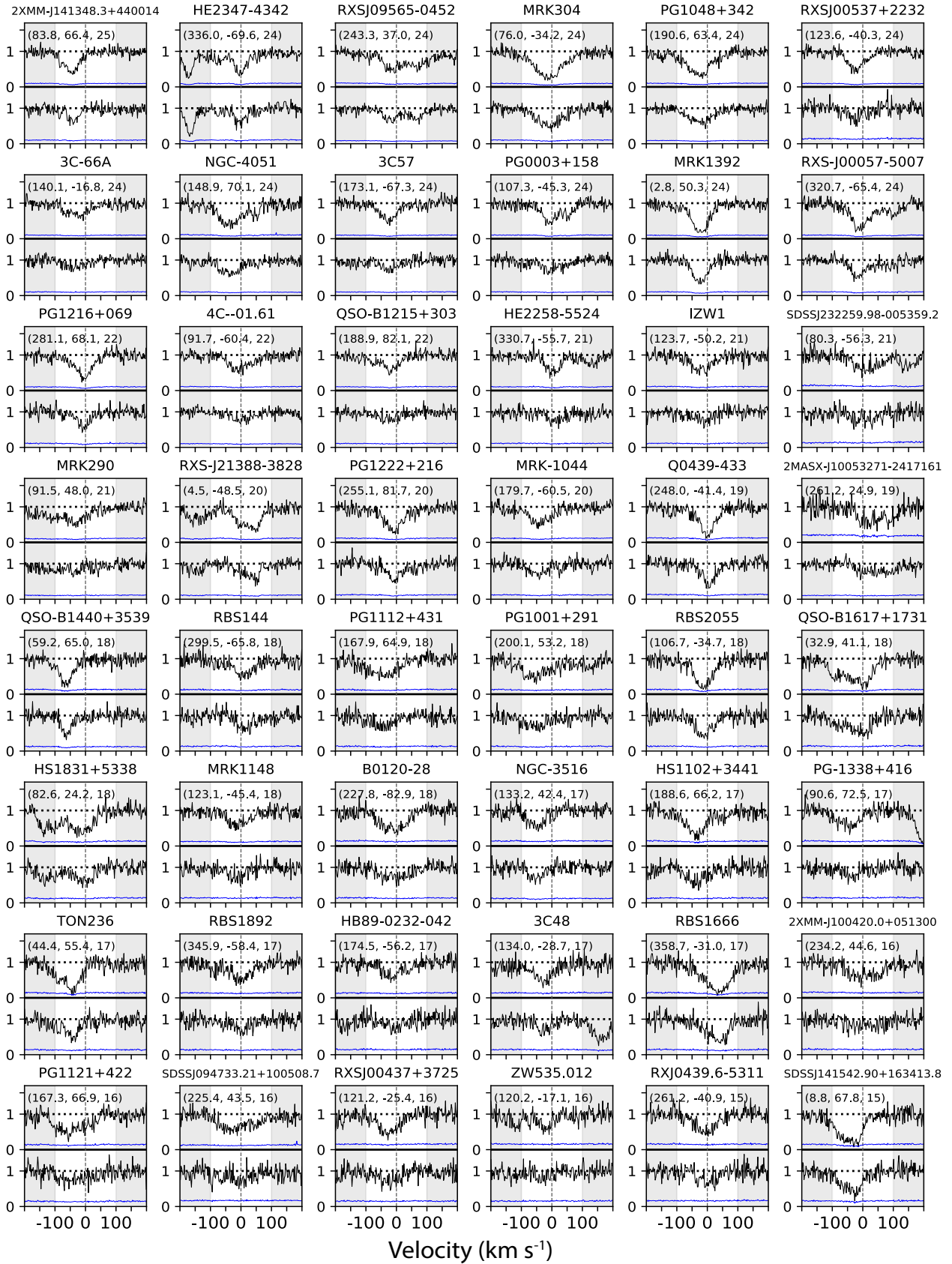


Figure 1 continued.

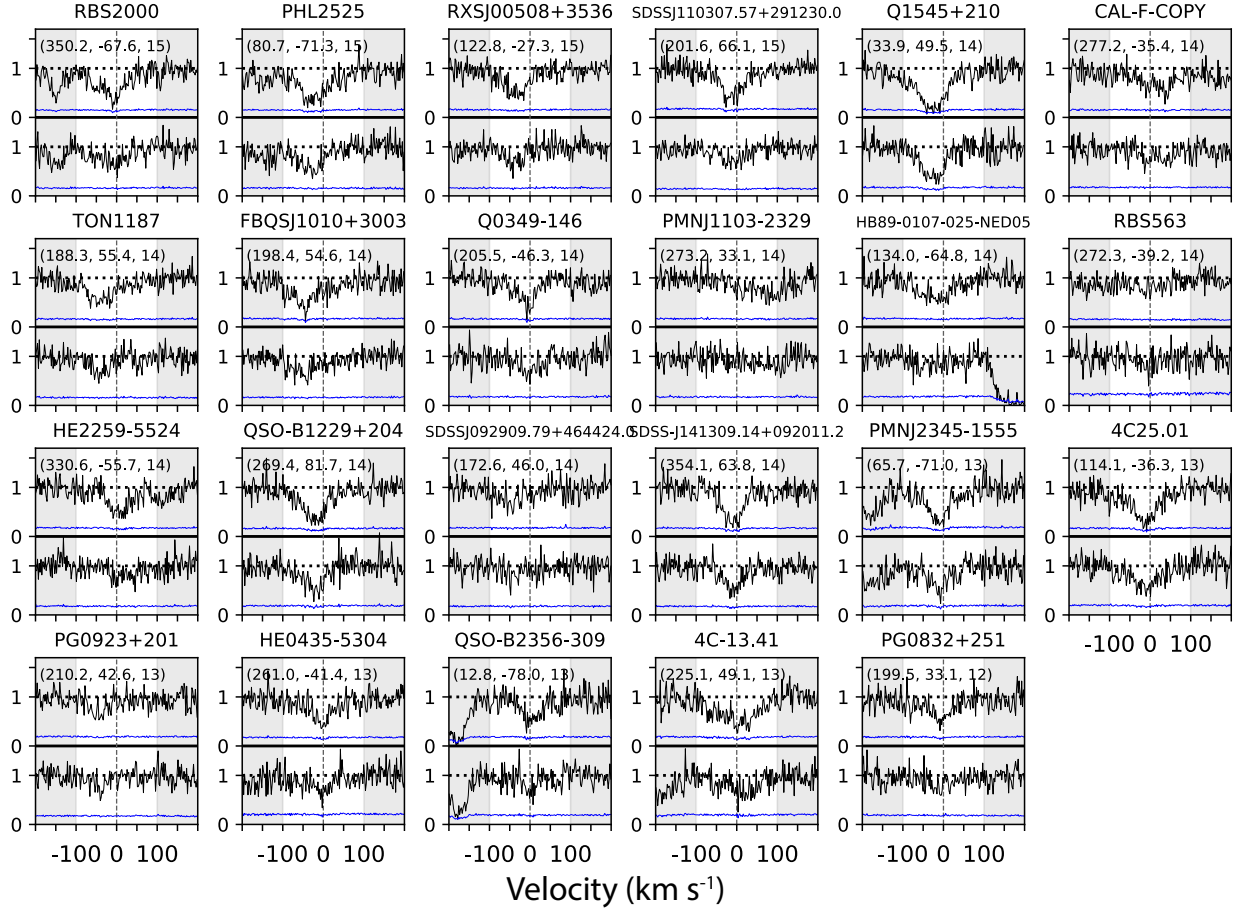


Figure 1 continued.

& Sembach 1991, 1996):

$$N_{\lambda}(v) = \frac{m_e c}{\pi e^2} \frac{-\ln[F_n(v)]}{f\lambda} \\ = 3.768 \times 10^{14} \frac{-\ln[F_n(v)]}{f\lambda(A)} [\text{atoms cm}^{-2}(\text{km s}^{-1})^{-1}],$$

$$N_{\lambda} = \int_{v_-}^{v_+} N_{\lambda}(v) dv,$$

$$v_{\lambda} = \int_{v_-}^{v_+} v N_{\lambda}(v) dv / \int_{v_-}^{v_+} N_{\lambda}(v) dv,$$

(2)

where  $F_n(v)$  is the continuum-normalized spectrum,  $\lambda$  is the line rest-frame wavelength, and  $f$  is the oscillator strength. We adopt  $\lambda=1393.76/1402.77 \text{ \AA}$  and  $f=0.513/0.254$  for the Si IV doublet from Morton (2003).  $N_{\lambda}$  is the total column density integrated over  $[v_{\min}, v_{\max}]$ , and  $v_{\lambda}$  is the flux-weighted centroid velocity. We adopt  $v_- = -100 \text{ km s}^{-1}$  and  $v_+ = +100 \text{ km s}^{-1}$ , respectively, as can be seen from Figures 1 and 2 that the majority of the MW Si IV absorption features occur within this velocity range. The column densities and centroid velocities are tabulated in Table 1.

Among the 132 QSOs, we found 16 sightlines<sup>6</sup> in

<sup>6</sup> They are with No. of 1, 2, 3, 4, 6, 7, 9, 14, 17, 19, 22, 24, 28, 36, 61, and 82 in Table 1.

common with the *Far-Ultraviolet Spectroscopic Explorer* sightlines used in Wakker et al. (2012; henceforth W12). For these sightlines, we calculate the integrated column density over the same velocity ranges as those adopted in W12. We find that the mean differences between our COS values and theirs are 0.05 dex for Si IV 1393Å and 0.07 dex for Si IV 1402Å, indicating that our continuum fitting and column-density measurements are consistent with literature values.

Even though the absorption-line profiles appear to be shallow, there might still exist spectrally unresolved saturation, as is pointed out by Savage & Sembach (1991). This effect is most significant when the full width half maximum (FWHM) of a strong absorption line is comparable to or smaller than the FWHM of the instrument's line-spread function. The unresolved saturation can also occur if multiple absorption components with various line widths coexist at similar velocity regions; the original absorption-line profiles end up being smeared into broader but shallower profiles. For ions with more than one transition line, they suggested an efficient way to identify unresolved saturation, which is to compare the

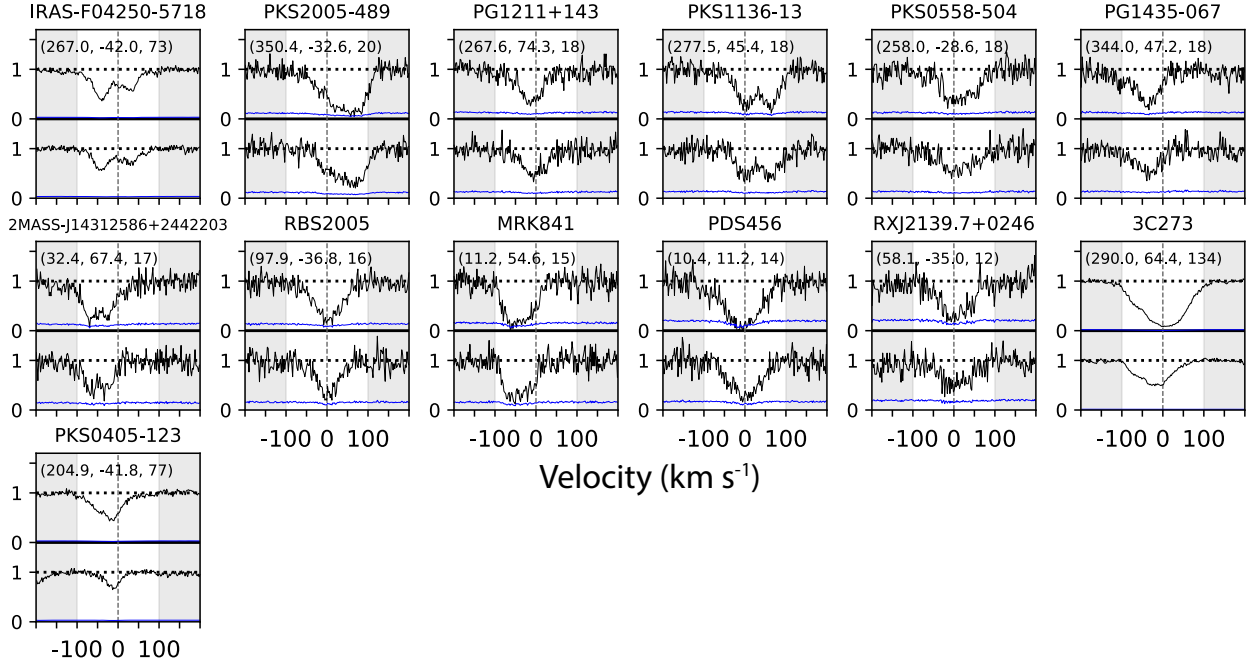


**Figure 2:** Same as Figure 1, but for the 11 sightlines with unresolved saturation ( $Q = 1$ ; noted with “S”) and the two sightlines with abnormally strong Si IV 1393 Å profiles ( $Q = -1$ ). See § 2.2 for more details.

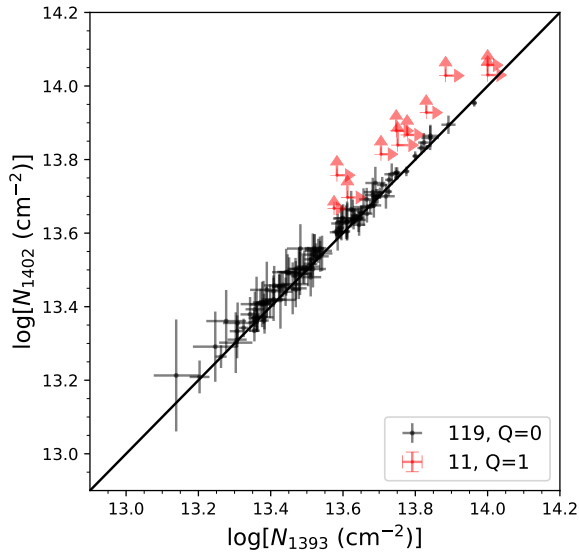


**Figure 3:** Comparison of Si IV doublet column-density measurements. In black are the 119 QSOs with spectrally resolved doublet profiles ( $Q=0$ ), which meets the criterion in Equation 3. In red are the 11 sightlines with unresolved saturation ( $Q=1$ ; see § 2.2).

$N_\lambda(v)$  profiles or the integrated  $N_\lambda$  values between the transition lines. A spectrally well-resolved target should yield consistent  $N_\lambda$  values among multiple absorption lines. Following this method, we define a QSO’s Si iv

doublet as spectrally well-resolved (i.e., unsaturated) if the column densities of the doublet are consistent within their combined quadrature error:

$$\begin{aligned} \delta \log N &\equiv |\log N_{1393} - \log N_{1402}| \leq \sigma_c, \\ \sigma_c &\equiv (\sigma_{1393}^2 + \sigma_{1402}^2)^{\frac{1}{2}}, \end{aligned} \quad (3)$$

where  $\sigma_c$  is the combined quadrature error, and  $\sigma_{1393}$  and  $\sigma_{1402}$  are the logarithmic errors of the corresponding  $\log N_{1393}$  and  $\log N_{1402}$  values as calculated from the spectra’s error arrays. In addition, we require that an unsaturated Si IV line should have its minimum normalized flux  $\geq 0.1$  because COS spectra are empirically known to be saturated when the normalized flux is lower than 0.1. The two requirements together find 119 (of 132) QSOs with unsaturated Si IV doublets, which we classify as  $Q = 0$ . The normalized doublet spectra are displayed in Figure 1, and their doublet column densities are shown as black symbols in Figure 3.

For the remaining QSOs, 11 of them either do not satisfy Equation 3 or the minimum fluxes of the spectra are lower than 0.1. We flag these QSOs as spectrally saturated with  $Q=1$ , and show their doublet spectra in Figure 2. The column-density measurements for these QSOs are shown as red crosses in Figure 3, from which we find that saturation mostly occurs at high column densities. Savage & Sembach (1991) provide column-density correction for unresolved saturated lines, which is based on a simulation of an isolated Gaussian component being

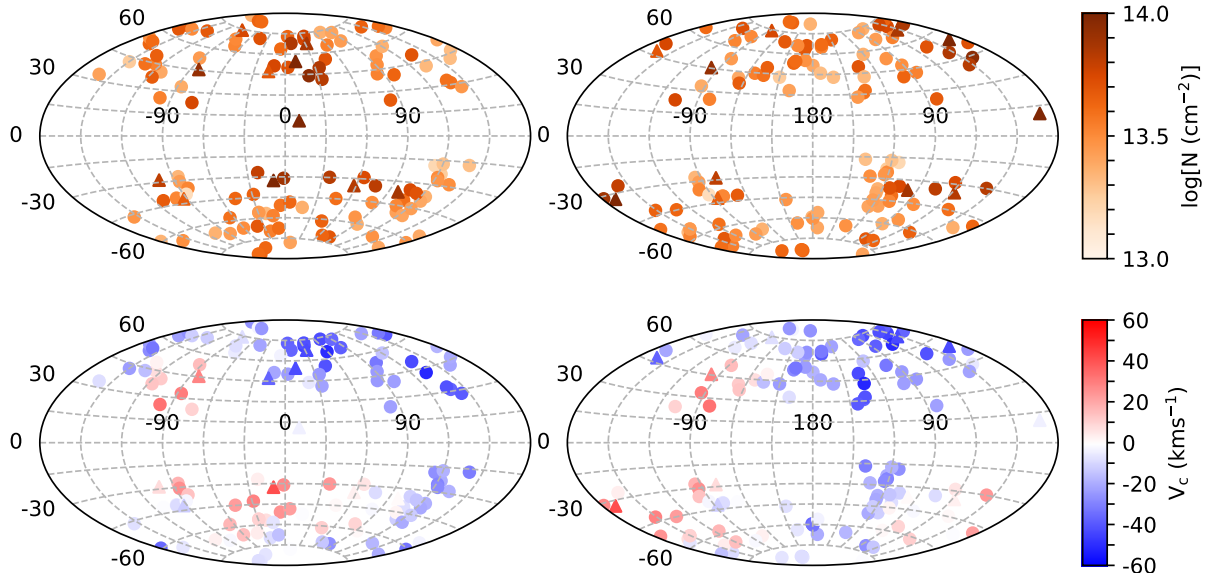


**Figure 4:** The top two panels show the column-density distribution of the low-intermediate velocity Si IV, with the left panel centered at the Galactic center and the right panel at anti-Galactic center. For spectrally non-saturated ( $Q = 0$ ) sightlines we show the mean column density of the doublet in dots; for spectrally saturated ( $Q = 1$ ) sightlines, we show the  $\log N_{1402}$  values as lower limits in upward triangles, given that Si IV 1402Å is weaker and, thus, is less saturated than 1393Å. The bottom two panels show the distribution of the mean centroid velocity  $v_c$  (see § 3).

smearred by instrument’s line-spread function with different FWHM. As they pointed out, the corrections are most precise if the doublet’s logarithm column-density difference is less than 0.05 dex. For targets with larger difference, the column-density correction itself could vary up to 0.1–0.3 dex if the lines have multiple components. Given that our  $\log N$  measurement errors are typically  $\sim 0.05$  dex and that there could be multiple components in the Si IV profiles as shown in Figure 2, it is unrealistic to apply column-density correction to these 11 saturated sightlines. We only list their column densities as lower limits in Table 1.

There remain two QSOs, 3C273 and PKS0405-123, which have  $\log N_{1393}$  values more than  $1\sigma_c$  higher than the  $\log N_{1402}$  values. Their spectra are shown in the last two panels in Figure 2. For 3C273, W12 suggests that the 1393 Å line may suffer from blending with Ly $\alpha$ . For PKS0405-123, we measure  $\log N_{1393} = 13.46 \pm 0.01$ , consistent with W12’s STIS–E140M value of  $\log N_{1393} = 13.43 \pm 0.04$ ; note that the QSO is listed as PKS0405-12 in their work. However, for 1402 Å we find  $\log N_{1402} = 13.25 \pm 0.02$  while W12 find  $13.40 \pm .07$ . Neither line shows signs of a peculiar profile in our COS spectra (Figure 2) despite the  $\log N$  difference. As W12 did not present the original spectra of PKS0405-123 in their work, we cannot conduct a close inspection of the line profiles to further compare results. We tag these two QSOs as  $Q=-1$ , and do not use them for future analyses.

### 3. THE ALL-SKY DISTRIBUTION OF Si IV WITH $|V_{\text{LSR}}| \leq 100 \text{ km s}^{-1}$

In this section we study the column density ( $\log N$ ) and centroid velocity ( $v_c$ ) distribution of Si IV moving at  $|v_{\text{LSR}}| \leq 100 \text{ km s}^{-1}$  over the Galactic sky, which we refer to as the *low-intermediate velocity* Si IV. Overall the north and south are roughly evenly sampled with 62 and 68 QSO sightlines, respectively. In the top two panels of Figure 4 and the left two panels of Figure 5, we show the mean doublet column densities of non-saturated ( $Q=0$ ) sightlines in dots, and show the  $\log N_{1402}$  values of saturated ( $Q=1$ ) sightlines in upper triangles to indicate the lower limits. For non-saturated ( $Q=0$ ) sightlines, we find a mean column density and a standard deviation value of  $\log N = 13.58 \pm 0.16$  dex [i.e.,  $N = (3.8 \pm 1.4) \times 10^{13} \text{ cm}^{-2}$ ].

We find that the column densities of sightlines toward the Galactic center ( $|l| \lesssim 30^\circ$ ) are generally 0.1–0.2 dex higher than those in other regions, as shown in panel 1a in Figure 5. This could be due to material associated with the boundaries of the north and south Fermi Bubbles (Ackermann et al. 2014; Fox et al. 2015; Bordoloi et al. 2017). Except for these sightlines, we do not see much difference between sightlines toward the inner ( $l \leq 90^\circ$  or  $l \geq 90^\circ$ ) or outer ( $90^\circ \leq l \leq 270^\circ$ ) Galaxy (see Panel 1b in Figure 5). And, we find that the northern and southern sky has similar Si IV column-density distribution, which is different from the obser-



vations of the low-intermediate velocity O VI studied by [Savage et al. \(2003\)](#). There they found that the column density of O VI at  $b > 45^\circ$  is  $\sim 0.25$  dex higher than those in other regions. Note that the column densities of both the northern and southern sightlines show little dependence on  $b$  as can be seen in panel 1b in [Figure 5](#), which provides a critical constraint on the models that we discuss in [§ 4.1](#) and [§ 4.2](#).

In the bottom two panels of [Figure 4](#) and the right two panels of [Figure 5](#), we show the mean centroid velocities for both non-saturated ( $Q=0$ ; dots) and saturated ( $Q=1$ ; triangles) sightlines. We find that the blue-shifted pattern near  $l \sim 180^\circ$  in panel 2a of [Figure 5](#) cannot be simply explained by co-rotation or halo lagging of ionized gas at the MW's disk-halo interface, which would otherwise show a clear segregation pattern of blue- and red-shifted velocity at  $l = 180^\circ$  ([Wakker 2004](#)). In panel 2b, most sightlines in the north show Si IV moving toward us at  $-50 \lesssim v \lesssim 0$  km s $^{-1}$ . Since these sightlines are mostly at  $b > 30^\circ$ , their centroid velocities suffer only modest projection effects. The blue-shifted gas implies an excess of inflowing gas toward the disk; in the south, no obvious trend of gas inflows is found. This north-south dichotomy of velocity has also been observed in intermediate velocity clouds in H I 21cm emission lines and metal absorption lines (e.g., [Wakker et al. 2001](#); [Schwarz & de Boer 2004](#); [Wakker 2004](#); [Richter 2017](#)). We also note that the segregation of inner and outer Galaxy sightlines at  $b < 0^\circ$  is likely an illustration artifact, as we do not find such sharp transition in the bottom right panel in [Figure 4](#) where smooth velocity field can be seen over the sky.

As we detect Si IV absorbers along every sightline, the covering fraction (i.e., detection rate) of the low-intermediate velocity Si IV at  $|b| \gtrsim 30^\circ$  is  $C_f=100\%$ . This is similar to the results of ionized high-velocity gas ([Fox et al. 2006](#); [Shull et al. 2009](#); [Collins et al. 2009](#); [Lehner et al. 2012](#); [Richter 2017](#)). For example, [Shull et al. \(2009\)](#) show that  $81\% \pm 5\%$  of the Galactic sky is covered by ionized high-velocity clouds according to a search of Si III absorbers in *HST*/COS and *FUSE* spectra of 37 AGNs, whereas [Richter \(2017\)](#) found a covering fraction of 74% for high-velocity Si III using COS observations. With a different set of ions (e.g., C II, C IV, Si III, Si IV), [Lehner et al. \(2012\)](#) found a covering fraction of 68% for gas moving at  $|v| > 90$  km s $^{-1}$  at  $|b| > 20^\circ$ . We discuss the implication of the high covering fraction in [§ 5.3](#).

#### 4. MODELS FOR THE Si IV ALL-SKY DISTRIBUTION

Without distance constraints, it is difficult to trace the origins of the low-intermediate velocity Si IV. In [§ 4.1](#), we briefly review a commonly adopted plane-parallel flat-

slab model which attributes the low-intermediate velocity Si IV to the MW's disk-halo interface (e.g., [Savage et al. 1990](#); [SW09](#); [W12](#)). Then in [§ 4.2](#), we propose a better-fit two-component model which includes a global component in addition to the flat-slab geometry to account for the flat but scattered Si IV column-density distribution as seen in panel 1b in [Figure 5](#).

##### 4.1. A Commonly Adopted Flat-Slab Model

The flat-slab model assumes a simple physical scenario that most of the low-intermediate velocity Si IV is related to the MW's disk-halo interface (e.g., [Savage et al. 1990](#); [Savage & Wakker 2009](#), henceforth [SW09](#); [W12](#)). The flat slab has an exponential density profile,  $n(z) = n_0 e^{-|z|/z_h}$ , extending above and below the Galactic disk. In this equation,  $z$  is the vertical distance from the Galactic plane,  $z_h$  is the scale height of the gas, and  $n_0$  is the midplane number density.  $z_h$  and  $n_0$  can be constrained in the following way: for a star at height  $z_s$  from the Galactic plane, the modeled column density seen toward the star projected along the vertical direction is  $N_{\text{mod},\perp} = \int_0^{z_s} n(z) dz$ .  $N_{\text{mod},\perp}$  can then be related to the observed column density toward the star as  $N_{\text{mod},\perp} = N_{\text{obs}} \sin|b|$ , where  $b$  is the star's Galactic latitude. Because the number density of the flat slab decreases dramatically above  $z_h$ , the value of  $N_{\text{mod},\perp}$  flattens as we probe background targets at vertical distances much larger than  $z_h$ , such as stars in LMC/SMC and extragalactic QSO sightlines.

[SW09](#) modeled the distribution of warm-hot ionized gas moving at low-intermediate velocities over the Galactic sky using the flat-slab geometry. They collected the column densities of a number of ions (e.g., H I, Al III, Si IV, C IV, O VI) for 109 halo star sightlines and 30 QSO sightlines from the literature (e.g., [Jenkins 1978](#); [Lehner & Howk 2007](#); [Bowen et al. 2008](#); [W12](#); see [Table 2](#) of [SW09](#) for a complete list of references). Different authors have varied choices of velocity ranges over which the ion column densities were integrated, but the adopted ranges are all near  $[-100, 100]$  km s $^{-1}$ . [SW09](#) examined the  $\log(N_{\text{obs}} \sin|b|) - \log|z|$  relation, and found that  $\log(N_{\text{obs}} \sin|b|)$  increases with  $\log|z|$  for most of their halo star sightlines, and the relation reaches a plateau for stars beyond certain heights. We reproduce [SW09](#)'s flat-slab experiment using their published stellar/QSO Si IV data in [Figure 6](#). In the left panel, the filled black symbols show the stellar sightlines used in their flat-slab parameter fitting. Sightlines noted as open symbols were not considered in their fitting because of either prominent H II regions, X-ray sources, or supernova remnants along the lines of sight. They also excluded a halo star vZ 1182 at  $\log|z| \sim 1.0$  and  $b \sim 79^\circ$  because of the concern of contamination from the potential excess region near the north Galactic pole, as revealed by the O VI

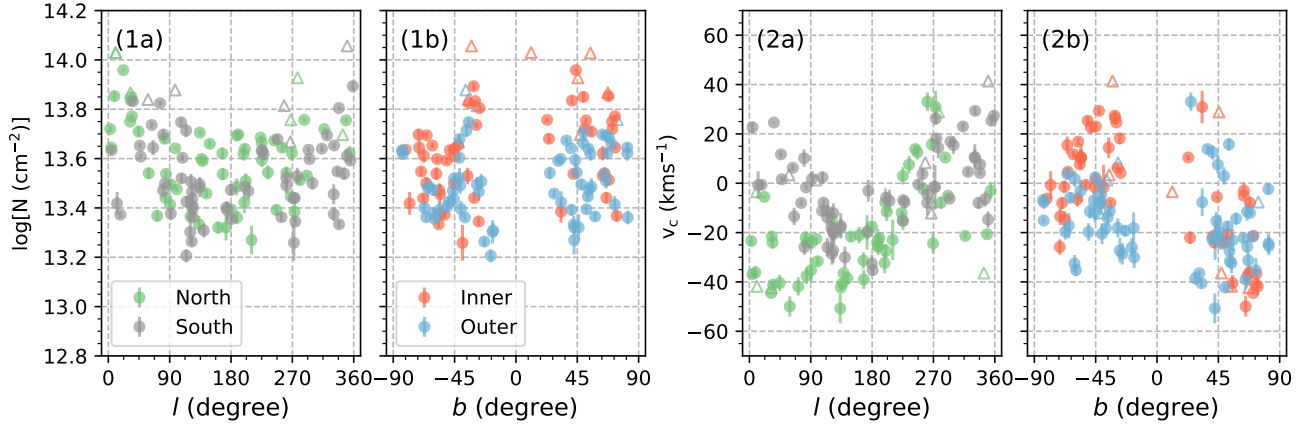


**Figure 5:** Panels 1a/1b show the  $\log N$  distribution as functions of  $l/b$ , respectively. For spectrally non-saturated ( $Q=0$ ) sightlines, we calculate the mean value of the doublet column density (dots); for spectrally saturated ( $Q=1$ ) sightlines, we show the  $\log N_{1402}$  value as lower limits (upward triangles). In panel 1a, we color-code the data into North ( $b > 0^\circ$ , green) and South ( $b \leq 0^\circ$ , grey); in panel 1b, we split the data into Inner ( $0^\circ < l < 90^\circ$  or  $270^\circ < l < 360^\circ$ , red) and Outer ( $90^\circ < l < 270^\circ$ , blue) sections. Panels 2a/2b show the  $v_c$  distribution as functions of  $l$  and  $b$ ; the symbols are color-coded the same way as those in panel 1a/1b, respectively. The centroid velocity is the mean of the doublet measurements for both the spectrally resolved and saturated sightlines.

all-sky distribution (Savage et al. 2003). The right panel shows the QSO measurements as a function of Galactic latitude. The 15 QSOs shown in filled circles were used in their modelling, and there are ten sightlines at  $b > 45^\circ$  (open circles) that were discarded to avoid the O VI-enhanced region near the north Galactic pole (Savage et al. 2003). The straight line and shaded area spanning from the left to the right panels in Figure 6 show their model prediction of the  $\log N_{\text{mod},\perp} - \log |z|$  relation. They found a best-fit scale height of  $z_h = 3.2_{-0.6}^{+1.0}$  kpc and mid-plane density of  $n_0 = 2.3 \times 10^{-9} \text{ cm}^{-3}$  for the Si IV flat slab.

Figure 6 shows that the flat-slab model is able to reproduce the general trend of the projected Si IV column densities seen toward halo stars. Since the model regards QSO sightlines as those with path lengths of infinity, the  $\log(N_{\text{obs}} \sin |b|)$  values from QSOs should always be  $\log(N_{\text{obs}} \sin |b|) = \log(n_0 z_h) = 13.36$  (SW09). However, we find that this constant value cannot describe the all-sky QSO measurements. A Spearman test of  $\log(N_{\text{obs}} \sin |b|) - |b|$  for our data (red symbols in the right panel) finds a correlation coefficient of  $r_s = 0.55^7$ , implying  $\log(N_{\text{obs}} \sin |b|)$  is likely to increase monotonically with  $|b|$ , which indicates that a flat-slab geometry with an exponential density distribution is not adequate to explain the Si IV content along QSO sightlines.

The mismatch between our QSO measurements and SW09’s flat-slab model prediction is further illustrated in Figure 7, where we directly compare the column-density

values without  $\sin |b|$  projection. The black curves and gray shades show the  $\log N$  prediction from SW09’s best-fit flat-slab model, which suggests a strong dependence of  $\log N$  on  $b$ , i.e., QSO sightlines near polar regions have the shortest path lengths through the flat slab and thus should have the least Si IV, while those near the Galactic plane have the longest paths and thus the most Si IV. However, the observed  $\log N$  does not follow this predicted trend –  $\log N$  seems to have a flat but scattered distribution regardless of sightlines’ Galactic latitudes. The right panel shows the column-density residuals between the QSO data and SW09’s flat-slab model prediction. A good model fit should yield residuals that randomly scatter around 0.0 dex, which is not the case here. The flat-slab model over-predicts  $\log N$  at low  $b$  and under-predicts those sightlines at high  $b$ , resulting in an increasing  $\delta \log N$  at higher  $b$ .

We note that this mis-match between the measured  $\log N$  and flat-slab prediction has also been found in studies of Galactic O VI (figure 12 of Savage et al. 2003) and C IV (figure 8 of W12) moving at low-intermediate velocities. In their work, Savage et al. (2003) analyzed *FUSE* spectra of 100 extragalactic targets and pointed out that a symmetrical flat slab with an exponential density profile cannot accurately depict the distribution of O VI moving at  $|v| \lesssim 100 \text{ km s}^{-1}$ . They also found that the O VI centroid velocities do not fit into the scenario of a flat slab co-rotating with the Galactic disk. C IV is likely to be a better proxy than O VI for Si IV given their comparable ionization potentials (33eV for Si IV and 48eV for C IV). In the flat-slab model, SW09 found a scale

<sup>7</sup> A separate test for north- and south-only sightlines finds  $r_{s,n} = 0.53$  and  $r_{s,s} = 0.54$ .

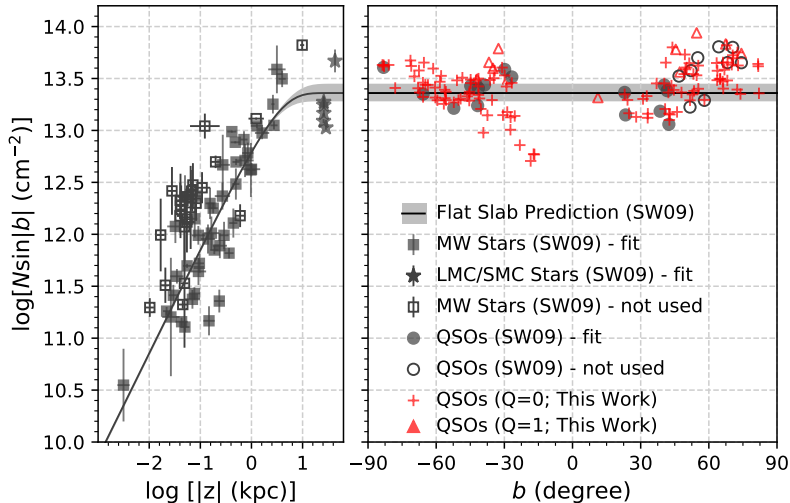


**Figure 6:** The  $\log(N\sin|b|)$ - $\log|z|$  relation for stellar sightlines on the left panel and for QSOs on the right, respectively. In the left panel, the filled black symbols were used by SW09 in their flat-slab model fitting, including 44 MW halo stars (squares) and six LMC/SMC stellar sightlines (stars). Open symbols show those targets excluded from fitting, owing to sightlines intercepting specific ISM/halo structures. This plot is adopted from the Si IV panel of figure 2 in SW09, although we do not include their upper/lower limit data. In the right panel, the red crosses/upward triangles are our Si IV measurements of spectrally resolved ( $Q=0$ )/saturated ( $Q=1$ ) sightlines, respectively; error bars are approximately equal to the size of the symbol. The black curve and gray shaded regions spanning from the left to the right panels show the predicted  $\log N_{\text{mod},\perp}$  and  $1\sigma$  values from SW09’s flat-slab model. Our QSO data show that  $\log(N\sin|b|)$  increases as  $|b|$  increases, which cannot be explained by the flat-slab geometry. See § 4.1 for more details.

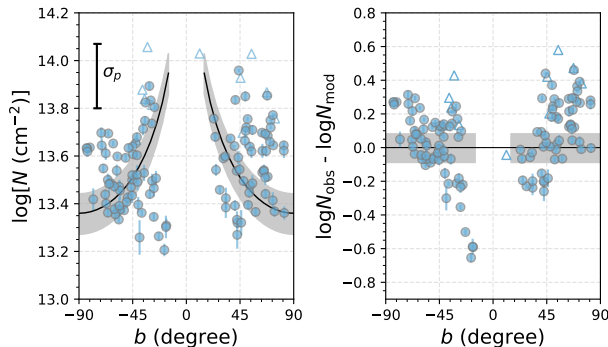


**Figure 7:** Left:  $\log N$ - $b$  relation for the low-intermediate velocity Si IV. The data points are the same as those in Figure 5, but here we do not separate the inner or outer Galaxy data points because no significant trend related to these two segments is seen. Black curves show SW09’s flat-slab model prediction, and the gray shades are the  $1\sigma$  ranges. The  $\sigma_p=0.27$  dex in the top left is the patchiness parameter that SW09 adopted, which we discuss in § 4.2. Right: Residuals of the observed and model-predicted Si IV column densities. A good model fit should yield a random distribution around 0.0 dex, however, the actual residuals show that the flat-slab model overpredicts the  $\log N$  value at low  $b$  and underpredicts those at high  $b$ .

height of  $z_h = 3.6$  kpc for C IV, which is similar to Si IV’s scale height of 3.2 kpc. W12 show their  $\log N$  measurements of C IV at low-intermediate velocity in their figure 8, overplotted with SW09’s flat-slab predictions. Their northern sightlines show a data-model mismatch similar to what we show in Figure 7. Their southern sightlines follow the general trend of the flat slab; however, because they have only 13 sightlines in the south, it is hard to clearly declare a  $1/\sin|b|$  effect.

To summarize, the flat-slab geometry cannot fully describe the low-intermediate velocity Si IV distribution seen along QSO sightlines. We proceed with a new model for the Si IV distribution by adding in a global component to the flat-slab model in § 4.2. Then we discuss the caveats of the flat-slab model and our model in § 5.1.

#### 4.2. A Two-Component Model

The spectrum of a QSO sightline going through the Galactic halo is likely to contain absorption-line information from the ISM, disk-halo interface, and the MW’s CGM in a large volume simultaneously. The ISM is unlikely to contribute much to the Si IV column density, as we discuss in § 5.2. Here we construct a *two-component* model to evaluate the contribution of a disk-halo flat slab and a global component to the line-of-sight column densities. The disk-halo component takes into account the

potential effect of Galactic latitude on a sightline’s Si IV column density: at low  $b$ , material at the disk-halo interface dominates the column density owing to a substantially increased path length through it (a factor of 2 for gas at  $b = 30^\circ$  compared to those at  $b = 90^\circ$ ). The global component reflects a uniform background to account for the weak  $b$  dependence as shown in Figure 5. In the following, we describe the model setup and solve for the model parameters using a Bayesian analysis in § 4.2.1. Our analysis follows the model-fitting discussion by Hogg et al. (2010) and the Bayesian framework discussion in chapter 5.6 in Ivezić et al. (2014). Then in § 4.2.2 we re-sample the all-sky sightlines using block bootstrapping to estimate the influence of potential large-scale structures on our results.

#### 4.2.1. Bayesian Analysis on the Original Data Set

We assume that the disk-halo and the global component contribute to the (LOS) column density linearly:

$$N = N_{\text{DH}}^\perp \times \frac{1}{\sin|b|} + N_{\text{G}}, \quad (4)$$

where  $N_{\text{DH}}^\perp$  is the column density of the disk-halo component projected onto the direction perpendicular to the Galactic plane. According to the flat-slab model (see § 4.1),  $N_{\text{DH}}^\perp$  should be a constant from sightline to sightline.  $N_{\text{G}}$  is the uniform global background, which is deemed invariant as well.

For a sightline  $k$  with column density  $N_k$ , we assume the measurement error  $e_k$  is Gaussian. The probability distribution function (pdf) for a sightline with  $N_k \pm e_k$  measurement given the two-component model is:

$$p_{\text{model}}(N_k, e_k | N_{\text{DH}}^\perp, N_{\text{G}}) = \frac{1}{\sqrt{2\pi}e_k} \exp\left[-\frac{(N_k - N_{\text{mod},k})^2}{2e_k^2}\right], \quad (5)$$

where  $N_{\text{mod},k} \equiv N_{\text{DH}}^\perp / \sin|b_k| + N_{\text{G}}$ . In addition, we assume the data are drawn from an intrinsic Gaussian distribution with zero mean and variance of  $\sigma_p^2$ , where  $\sigma_p$  is termed as the patchiness parameter. This assumption is to account for the scatter seen in the column-density measurements in Figure 5 and § 3, which is an order of magnitude larger than the measurement errors  $\{e_k\}$ . We discuss the physical meaning of  $\sigma_p$  and its difference from the patchiness parameter used in SW09 in § 5.1. We can write down the probability of a sightline with column density  $N_k$  drawn from an intrinsic  $(0, \sigma_p^2)$  distribution:

$$p_{\text{scatter}}(N_k | \sigma_p) = \frac{1}{\sqrt{2\pi}\sigma_p} \exp\left(-\frac{N_k^2}{2\sigma_p^2}\right). \quad (6)$$

We convolve Equations 5 and 6 to find the probability of a sightline  $N_k$  following a linear relation (Equation 4)

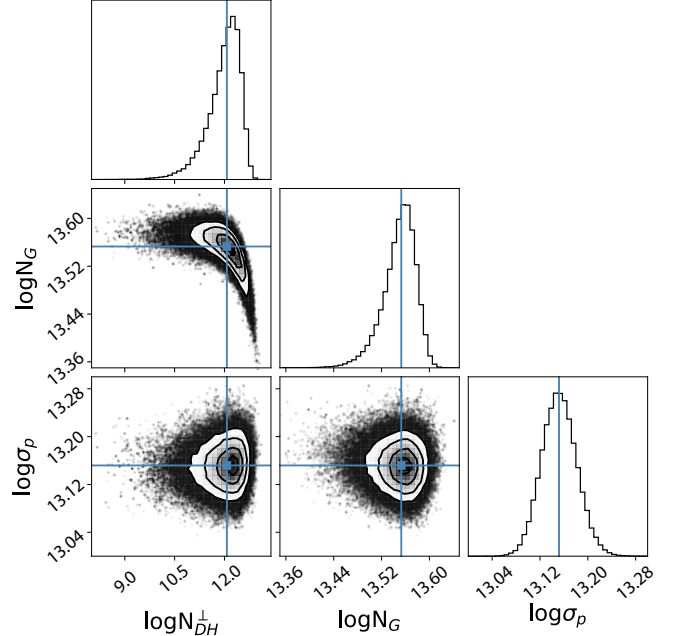


**Figure 8:** The 1D and 2D marginalized posterior distributions for the parameters  $N_{\text{DH}}^\perp$ ,  $N_{\text{G}}$ , and  $\sigma_p$ . Note the large range differences on the axes for the three parameters. The blue lines show the 50th percentile values for the parameters. This plot is generated with [corner.py](https://corner.py) (Foreman-Mackey 2016).

with a Gaussian intrinsic scatter:

$$p(N_k, e_k | N_{\text{DH}}^\perp, N_{\text{G}}, \sigma_p) = p_{\text{model}} * p_{\text{scatter}} = \frac{1}{\sqrt{2\pi}(e_k^2 + \sigma_p^2)} \exp\left[-\frac{(N_k - N_{\text{mod},k})^2}{2(e_k^2 + \sigma_p^2)}\right]. \quad (7)$$

For brevity, we define  $\theta \equiv (N_{\text{DH}}^\perp, N_{\text{G}}, \sigma_p)$  as the parameter set in the following.

Because our dataset includes  $K=119$  QSO sightlines with non-saturated Si IV doublets, we can calculate the likelihood of all these sightlines’ LOS column densities being drawn from the two-component model with Gaussian intrinsic scatter as:

$$\mathcal{L} = \prod_{k=1}^K p(N_k, e_k | \theta). \quad (8)$$

A general approach to solve for the best-fit parameter set is to maximize  $\mathcal{L}$  (or to minimize the logarithmic value,  $\ln \mathcal{L}$ ). However, this maximum-likelihood method does not take into account a prior knowledge that the parameters  $(N_{\text{DH}}^\perp, N_{\text{G}}, \theta)$  should have nonnegative values to yield physical meanings. The prior regarding this information can be written as:

$$p(\theta | I) = \begin{cases} \text{const.} & N_{\text{DH}}^\perp \geq 0 \ \& \ N_{\text{G}} \geq 0 \ \& \ \sigma_p \geq 0, \\ 0.0 & \text{other cases,} \end{cases} \quad (9)$$

where the exact value of the constant is not important because we can renormalize over the posterior marginal pdf later. We can combine  $p(\theta|I)$  with  $\mathcal{L}$  to construct the posterior pdf for  $\theta$ :

$$p(\theta|\{N_k\}_{k=1}^K, I) = \frac{\mathcal{L} \times p(\theta|I)}{p(\{N_k\}_{k=1}^K|I)}, \quad (10)$$

The term in the denominator can be treated as a normalization constant so the integration for  $p(\theta|\{N_k\}_{k=1}^K, I)$  over the parameter space will yield unity. The denominator term is trivial in our analysis, so in the following we will use  $C$  to note any terms related to it. Conventionally, we calculate the logarithmic value of the posterior pdf:

$$\begin{aligned} \ln[p(\theta|\{N_k\}_{k=1}^K, I)] &= \ln\mathcal{L} + \ln[p(\theta|I)] + C \\ &= \sum_{k=1}^K \ln \frac{1}{\sqrt{2\pi(e_k^2 + \sigma_p^2)}} \\ &\quad - \sum_{k=1}^K \frac{(N_k - N_{\text{mod},k})^2}{2(e_k^2 + \sigma_p^2)} \\ &\quad + \ln[p(\theta|I)] + C. \end{aligned} \quad (11)$$

To solve for  $\ln[p(\theta|\{N_i\}_{i=1}^K, I)]$ , we sample over the parameter space  $(N_{\text{DH}}^\perp, N_G, \sigma_p)$  using the Markov chain Monte Carlo (MCMC) method with *emcee* (Foreman-Mackey et al. 2013), which is a Python implementation of the Affine Invariant MCMC Ensemble sampler (Goodman & Weare 2010). In Figure 8 we show the 1D and 2D marginalized distributions of the parameters. For the global component and the Gaussian intrinsic scatter, their posterior distributions show narrow profiles; we find the 50th percentile values at  $\log N_G = 13.55$ , and  $\log \sigma_p = 13.15$ . For the disk-halo component, we find a broader distribution over a dynamic range of  $\sim(9, 13)$ ; the 50th percentile is  $\log N_{\text{DH}}^\perp = 12.07$ . Figure 8 shows that our modeling yields better constraints for  $N_G$  and  $\sigma_p$  than for  $N_{\text{DH}}^\perp$ . This is likely to be due to the distribution of QSOs in our data set: because most QSOs are located at  $|b| > 30^\circ$  (see Figure 4), the LOS column density is dominated by the global component, whereas the disk-halo component only becomes prominent at lower Galactic latitudes as a result of increased path length through the flat-slab medium (see § 5.1 for discussion on model caveats).

#### 4.2.2. Block Bootstrapping Over the Galactic Sky

Our previous analysis makes the implicit assumption that the sightlines are independent and uniformly distributed, which is not a well-defined assumption, because the gaseous Galactic sky is covered by various structures, such as the large complexes moving at intermediate velocities in the northern sky (e.g., IV Arch and IV Spur; Wakker 2004) and the Fermi Bubbles. Although our data have sampled the north and south quite evenly (62 QSOs in the north and 68 in the south), it is possible that some

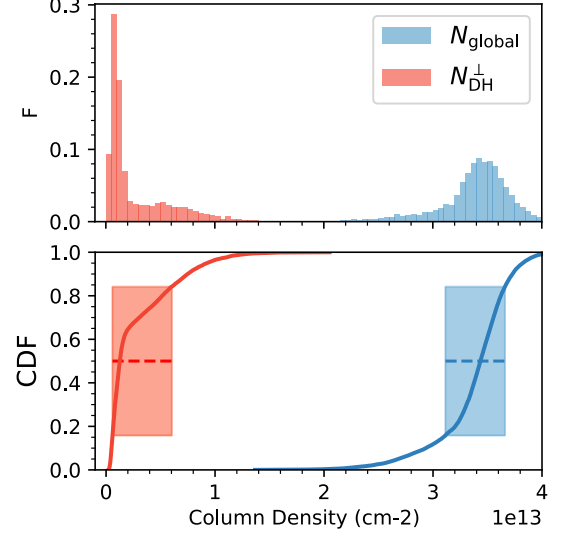


**Figure 9:** Top: distribution of the 50th percentile values of  $N_{\text{DH}}^\perp$  (red, left) and  $N_G$  (blue, right) from  $10^4$  runs of block bootstrapping. The data are binned in steps of  $5 \times 10^{11} \text{ cm}^{-2}$ . Bottom: The cumulative distribution function (CDF) for  $N_{\text{DH}}^\perp$  and  $N_G$ . The square patches show the  $1\sigma$  (68.2%) credible ranges.

sightlines are correlated at certain spatial scales. Here we divide the Galactic sky into eight segments: each segment is  $90^\circ \times 90^\circ$  in size, with the first segment at  $(l, b) = (0^\circ, -90^\circ)$ . By block bootstrapping these eight segments and rerunning the MCMC using the newly sampled datasets  $10^4$  times, we reduce the covariance due to very large structures.

For each run, we repeat the MCMC process and calculate the 50th percentile values of  $(N_{\text{DH}}^\perp, N_G, \sigma_p)$ . We show the distribution of the 50th percentile values for  $N_{\text{DH}}^\perp$  and  $N_G$  in Figure 9. In the top panel, the data are binned in steps of  $5 \times 10^{11} \text{ cm}^{-2}$  for both  $N_{\text{DH},\perp}$  and  $N_G$ . The disk-halo component  $N_{\text{DH},\perp}$  shows a sharp peak at low column-density values less than  $2 \times 10^{12} \text{ cm}^{-2}$ , whereas the global component  $N_G$  has a broad base with a peak at  $\sim 3.4 \times 10^{13} \text{ cm}^{-2}$ . We show the cumulative distribution functions (CDFs) of  $N_{\text{DH}}^\perp$  and  $N_G$  in the bottom panel. At the 68.2% confidence level ( $1\sigma$ ), we find  $N_{\text{DH}}^\perp = 1.3_{-0.7}^{+4.7} \times 10^{12} \text{ cm}^{-2}$  and  $N_G = 3.4_{-0.3}^{+0.3} \times 10^{13} \text{ cm}^{-2}$ . Similarly, we find the patchiness parameter  $\sigma_p$  has a median value of  $\sigma_p = 1.4 \times 10^{13} \text{ cm}^{-2}$ , consistent with the column-density scatter measured from the QSO data.

We compare our two-component best fit with the QSO measurements in Figure 10. At low Galactic latitudes where the LOS path goes deeply through the flat slab, the disk-halo component contributes to the majority of the column density; while at high Galactic latitudes, the global component dominates the LOS column densities.

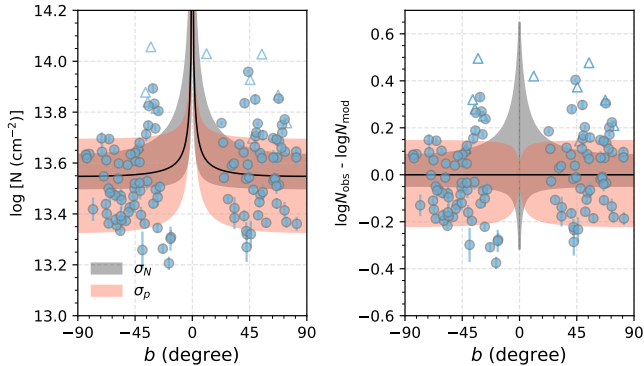


**Figure 10:** Left:  $\log N$ - $b$  distribution. The data points are the same as those in Figure 7. The black line shows the predicted column densities from our two-component model and the gray shades indicate the 68.2% ( $1\sigma$ ) confidence range as inferred from the CDF (Figure 9). The red shades show the patchiness parameters, which cover most of the data points, indicating that our model is able to account for the intrinsic scatter of the LOS column density. Right: column-density residuals of the observed and model-predicted Si IV column densities. A Spearman test on the data-model residuals finds a correlation coefficient of  $r_s = 0.13$ , implying that the abnormal trend of  $\delta \log N$  increasing with  $b$  seen in Figure 7 has now disappeared.

In addition, as highlighted in red shades, the Gaussian-form patchiness parameter we include in the model is able to recover most of the intrinsic column-density scatter in the data. Remarkably, the column-density residuals in the right panel now do not show any abnormal trend of  $\delta \log N$  increasing with  $b$ , indicating that our two-component model is likely a better representation of the Si IV seen toward QSOs than the commonly adopted flat-slab model. Because our model does not have distance information from the QSO sample, we cannot yield meaningful constraints on the spatial extensions of the disk-halo and global components. We discuss the potential origin(s) of the global component in § 5.2.

## 5. DISCUSSION

In the previous section, we briefly reviewed the commonly adopted flat-slab model and proposed a two-component model to better describe the all-sky distribution of Si IV absorption at low-intermediate velocity. Here, we first discuss the caveats of both models (§ 5.1). We proceed by discussing the potential origin(s) of the Si IV global component, which dominates over the disk-halo component in column density (§ 5.2). Finally, we conduct order-of-magnitude mass calculations for the global component in the context of the MW’s CGM (§ 5.3).

### 5.1. Caveats of the Models

A considerable degree of column-density scatter can be seen in both SW09’s star/QSO sample and our QSO sample, indicating that the Si IV-bearing gas is patchy. There are several reasons for the patchiness of a disk-halo and halo medium. For example, the Galactic fountain (Shapiro & Field 1976) that circulates material between the disk and halo may be responsible for some of the scatter. Along the trajectory of a fountain gas parcel, the gas may experience several phase changes due to different cooling rates at different locations (Marasco et al. 2012), resulting in a clumpy and inhomogeneous medium. Additional processes may also contribute to the column-density scatters, such as outflowing material from star-forming sites (e.g., Rubin et al. 2014), inflowing filaments from the halo (e.g., Zheng et al. 2017) as well as the debris of satellites passing through the Galactic halo (e.g., the Magellanic Stream; Nidever et al. 2010; Fox et al. 2014).

The concept of a patchiness parameter was originally introduced by SW09. To obtain the best parameters for their flat-slab disk-halo model, SW09 incorporated a fixed logarithmic  $\sigma_p$  value to their measurement errors so that the reduced  $\chi^2$  could be forced to 1.0 at their best fits. Without  $\sigma_p$ , the reduced  $\chi^2$  would be  $\gg 1.0$  and the best-fit parameters would be determined by those measurements with the smallest errors. In their setup,  $\sigma_p$  is a mathematical remedy for the oversimplified model fitting; however, it does not convey a clear physical meaning. Our two-component model defines the patchiness parameter  $\sigma_p$  as to reflect the intrinsic column-density scatter from sightline to sightline. The intrinsic scatter is assumed to follow a Gaussian distribution with a variance of  $\sigma_p^2$ . This setup of  $\sigma_p$  captures the large fluctuations in the dataset, however, it still lacks a physically motivated meaning of the nature of gas structures over the Galactic sky.

Another caveat pertaining to both SW09’s and our model is rooted in the sample selection. The halo stars in SW09 lie mostly at  $|b| < 15^\circ$  and toward the inner Galaxy direction (see their figure 1). Their sightlines at higher Galactic latitudes consist of 15 QSOs at  $b < 45^\circ$  and six stars in the LMC/SMC. Along the QSO and LMC/SMC stellar sightlines, the sources of and distances to the foreground low-intermediate velocity absorbers are not well-constrained. This inhomogeneous sample selection and the inclusion of distant QSOs and LMC/SMC stellar sightlines in their model fitting likely overestimate the flat-slab scale height. In contrast, our sample is dominated by QSOs at  $|b| \gtrsim 30^\circ$  (see Figures 4/5) and our two-component model does not have distance information on the gas as limited by the QSO data sample.

We note that our model finds a significant global back-

ground in addition to the disk-halo component, whereas SW09's flat-slab model does not include such a component. The inconsistency between the two models suggests that the gaseous structures of the MW cannot be simply parameterized by either a flat-slab or a global distribution. SW09's flat-slab model captures the properties of the MW's disk-halo interface at low Galactic latitudes, whereas our two-component model better represents the MW halo at higher latitudes. Ideally, the QSOs at high latitudes and stars near the Galactic plane should be combined to provide better modeling constraints on the distribution of the warm-ionized gas in the MW halo.

### 5.2. Origin(s) of the Si IV Global Component

Here we discuss the origin(s) of the global component revealed in § 4.2. We attempt to consider all of the possible ionized structures that the QSO paths may intercept.

First, we consider a Galactic ISM origin. It is unlikely that our QSO sightlines would suffer strong contamination from dense spiral-arm regions or warps at the outskirts of the MW's disk because the QSOs are mostly at  $|b| \gtrsim 30^\circ$ . However, all sightlines must leave the disk through the Local Bubble, a cavity in the ISM at the location of the Sun with a radius of  $\sim 100$  pc. SW09's halo star sample contains three objects within 1 kpc of the Sun (HD\_38666, HD\_52463, HD\_116658). The mean Si IV column density measured along these sightlines is  $\log N \sim 12.5$  dex, which accounts for only  $\sim 10\%$  of the Si IV toward distant QSOs. Furthermore, Savage & Lehner (2006) found that the local bubble contributes only  $\sim 9\%$  of the column density to the total O VI content in the MW halo by comparing UV spectra of nearby white dwarfs at a mean distance of  $\sim 109$  pc with those of MW halo stars. On the basis of this result, SW09 suggest that Si IV from the Local Bubble would not have a significant effect, despite the potential phase difference between the O VI- and Si IV-traced material.

Second, superbubbles breaking out of the ISM near the solar neighborhood are unlikely to be the source. This is primarily because the upstreaming material should be found with mostly positive radial velocities, in stark contrast to our velocity-centroid measurements (Figure 4) that predominantly trace negative radial velocities. However, it is possible that we are seeing the remnants of a past superbubble break-out, where the bulk of the previously ejected material is now falling back down. In this scenario, the fall-back gas is not distinguishable from the observed ionized intermediate- and high-velocity clouds, which we will discuss shortly.

Third, as our sightlines cover most of the Galactic sky at  $|b| \gtrsim 30^\circ$ , any particular substructures covering small areas of the sky cannot be the dominant sources, but are likely to contribute to the column-density scatter. The potential structures include: (1) the north and

south Fermi Bubbles (e.g., Fox et al. 2015; Bordoloi et al. 2017) which we have discussed in § 3, (2) the CGM of M31 in the southern sky (Lehner et al. 2015), and (3) cool filamentary structures embedded in the  $10^5 - 10^7$  K warm-hot intergalactic medium in the Local Group (e.g., Nicastro et al. 2003; Richter 2017). As we divide the sky into octants for block bootstrapping, the influence of sightlines potentially associated with small-area structures have been reflected in the distribution of the  $(N_{\text{DH},\perp}, N_{\text{G}})$  solutions (Figure 9).

Fourth, we consider that the global component may be associated with the widespread H I structures observed in the inner Galactic halo. Intermediate-velocity clouds are defined as discrete H I clouds moving at  $|v| < 100$  km s $^{-1}$  (van Woerden et al. 2004; Albert & Danly 2004; Wakker 2004) at distances of  $\sim 1 - 5$  kpc above the Galactic plane (see Table 2 in Albert & Danly 2004), and high-velocity clouds are those moving at  $|v| > 100$  km s $^{-1}$  at further distances around  $\sim 10$  kpc (van Woerden et al. 2004; Putman et al. 2012; Lehner et al. 2012; Richter 2017). Because we only consider the origin of the Si IV global component at low-intermediate velocities, ionized HVCs themselves are not the possible culprits; however, clouds have been found with properties similar to HVCs moving at lower velocities (Peek et al. 2009; Saul et al. 2014) as expected from models (Wakker 1991). If the global component represents the ionized counterparts of the IVCs or HVCs, one would expect the Si IV-bearing clouds to be distributed in a spherical configuration so that the column densities have minimal dependence on  $|b|$ .

Ultimately, we consider that the global component may represent a contribution from material occupying the MW's CGM, extending to  $\sim 0.5 R_{\text{vir}}$ . All QSO sightlines would intercept the extended CGM material of the MW. As mentioned in the Introduction, the MW's CGM is typically studied at high velocities ( $|v| > 100$  km s $^{-1}$ ) to avoid contamination from more nearby low-intermediate velocity gas (e.g., Fox et al. 2006; Shull et al. 2009; Collins et al. 2009; Lehner et al. 2012; Richter 2017). However, Zheng et al. (2015) found that  $\sim 65\%$  of the MW's CGM mass above  $|b| \geq 20^\circ$  is likely to be hidden at  $|v| \leq 100$  km s $^{-1}$  regardless of gas phases, according to a synthetic observation of a simulated MW-mass galaxy from a cosmological simulation (Joung et al. 2012). Empirically, as found in extragalactic CGM studies, highly ionized, metal-enriched gas can extend to nearly half the virial radii of the host galaxies with centroid velocities largely within  $|v| \lesssim 200$  km s $^{-1}$  of the systemic velocities (e.g., Werk et al. 2014; Liang & Chen 2014; Burchett et al. 2016; Keeney et al. 2017). Therefore, it is likely that the Si IV in the MW's CGM extends beyond the inner Galactic halo and casts absorption features in the low-intermediate velocity range.

To summarize, we find that the global component is unlikely to be dominated by the Local Bubble, superbubble breakouts, Fermi Bubble, M31’s CGM, or the Local Group medium. The global component is most likely to represent the ionized counterparts to nearby IVCs/HVCs, and/or the MW’s extended, ionized CGM that occupies a much larger volume, although its exact location is unknown. In each of these potential scenarios, spherical-like geometry better describes the data than the flat-slab cylindrical geometry because there is not an observed dependence on  $|b|$  for the Si IV column densities (Figures 5, 7, and 10). The dominant global component over the disk-halo component shows that there is likely to be a large amount of ionized gas moving at low-intermediate velocities hidden in the MW’s CGM.

### 5.3. Order-of-magnitude Calculation of the MW’s CGM Mass

Although our data show a covering fraction of 100% over the Galactic sky, the distance to the gas in the extended halo is unclear. As found in extragalactic work (Werk et al. 2013; Keeney et al. 2017), the radial profile of gas density in the CGM drops as a power law: the gas in the inner halo is denser than the gas in the outskirts. Werk et al. (2013) suggested that for star-forming galaxies with specific star formation rate  $\geq 10^{-11} \text{ yr}^{-1}$ , the covering fraction of Si IV is 94% within an impact parameter of  $\leq 75 \text{ kpc}$  but drops to 58% for regions between 75 and 160 kpc. This indicates that for observations of gas in the MW’s halo, the column density along the LOS is most likely to be dominated by nearby gas in the inner Galactic halo.

Here we conduct an order-of-magnitude estimate for the mass of the low-intermediate velocity Si IV-bearing gas in the MW’s CGM. We consider the case that the global component found in § 4.2 is associated with the MWs extended CGM in a spherical volume with a constant-density profile  $n(r) \equiv N_G/R$ , where  $R$  is the size of the halo. The total mass associated with this component is  $M_{\text{SiIV}} = \frac{4\pi}{3} R^3 (\frac{N_G}{R}) m_{\text{SiIV}} C_f$ , where  $N_G = 3.4 \times 10^{13} \text{ cm}^{-2}$  is the median column-density value of the global component we derived in § 4.2.2,  $m_{\text{SiIV}}$  the mass of a Si IV atom, and  $C_f = 100\%$  the covering fraction. For the radius, we adopt  $R = 75 \text{ kpc}$  on the basis of the covering fraction study of Werk et al. (2013), as mentioned above. The choice of  $R = 75 \text{ kpc}$  results in a conservative mass estimate for the Si IV-bearing gas in the MW’s CGM since there could be more diffuse gas beyond this volume but within the virial radius. The mass of the low-intermediate velocity Si IV in the MW’s CGM is:

$$M_{\text{SiIV}} \gtrsim 1.8 \times 10^5 M_\odot \left(\frac{R}{75 \text{ kpc}}\right)^2 \left(\frac{N_G}{3.4 \times 10^{13} \text{ cm}^{-2}}\right) \left(\frac{C_f}{1}\right). \quad (12)$$

We further convert the Si IV mass into a total gas mass by assuming that the Si IV-bearing gas represents the bulk property of the MW’s CGM at cool phases:

$$\begin{aligned} M_{\text{gas}} &= 1.4 m_{\text{H}} \left(\frac{M_{\text{SiIV}}}{m_{\text{Si}}}\right) f_{\text{SiIV}}^{-1} (\text{Si}/\text{H})_\odot^{-1} Z^{-1} \\ &\gtrsim 3.1 \times 10^9 M_\odot \left(\frac{f_{\text{SiIV}}}{0.3}\right)^{-1} \left(\frac{C_f}{1}\right) \left(\frac{R}{75 \text{ kpc}}\right)^2 \\ &\quad \left(\frac{Z}{0.3 Z_\odot}\right)^{-1} \left(\frac{N_G}{3.4 \times 10^{13} \text{ cm}^{-2}}\right), \end{aligned} \quad (13)$$

where 1.4 is to account for the presence of helium and  $m_{\text{H}}$  is the mass of a hydrogen atom. We adopt  $(\text{Si}/\text{H})_\odot = 10^{-4.49}$  from Asplund et al. (2009), which is the silicon abundance in the present-day solar photosphere relative to hydrogen. We assume the metallicity as  $Z = 0.3 Z_\odot$ , on the basis of the COS-Halos mean CGM metallicity estimate (Prochaska et al. 2017). The most uncertain term is the ionization fraction  $f_{\text{SiIV}}$ , defined as the ratio of Si IV to all the silicon in various neutral and ionized states. Photoionization, collisional ionization, and other non-equilibrium processes such as shock ionization, conductive interfaces, and turbulence mixing may contribute to producing Si IV (e.g., Fox et al. 2005; W12). We examine the ionization fraction produced by CLOUDY (v13.03; Ferland et al. 1998, 2013) in an extragalactic UV background (Haardt & Madau 2001) at H I column density of  $10^{20} \text{ cm}^{-2}$ , and find  $f_{\text{SiIV}}$  peaks at  $\sim 0.3$  for  $Z = 0.1 - 0.3 Z_\odot$ . This also results in a conservative mass estimate because we assume a maximum ionization fraction of Si IV. Because we only aim for an order-of-magnitude mass calculation, we do not conduct sophisticated ionization modelings to determine  $f_{\text{SiIV}}$ . We caution that the Si IV ionization fraction is highly uncertain without fully understanding its ionization mechanism (e.g. W12; Werk et al. 2016). Furthermore, metallicity measurements for the ionized gas are notoriously difficult to obtain. Large systematic uncertainties in gas ionization state, metallicity, and medium clumpiness plague all mass estimates based on ionized gas absorption lines. Therefore, our mass calculation for the MWs extended CGM is accurate only as an order-of-magnitude estimate.

Zheng et al. (2015) suggested that the mass ratio of high- to low-intermediate velocity gas in the MW halo at  $|b| \geq 20^\circ$  is 0.35 : 0.65 and this mass ratio does not vary significantly from 10 kpc to 250 kpc, on the basis of a synthetic observation of a simulated MW-mass galaxy. If we apply this ratio to the mass in Eqn. 12 and 13, we find the total Si IV and hydrogen mass in the MW’s CGM is,

$$\begin{aligned} M_{\text{SiIV,all}} &\gtrsim M_{\text{SiIV}}/0.65 \gtrsim 2.8 \times 10^5 M_\odot \\ M_{\text{gas,all}} &\gtrsim M_{\text{gas}}/0.65 \gtrsim 4.7 \times 10^9 M_\odot. \end{aligned} \quad (14)$$

In addition, we can infer the mass for the high-velocity gas ( $|v_{\text{LSR}}| > 100 \text{ km s}^{-1}$ ) at cool phases in the Galactic halo, which will be  $M_{\text{gas,hvc}} = 0.35 M_{\text{gas,all}} \gtrsim 1.7 \times 10^9 M_\odot$ . When compared to the literature, We



find that  $M_{\text{gas,hvc}}$  is consistent with the mass estimate for the MW's ionized HVCs including the Magellanic Stream ( $M \geq 3.0 \times 10^9 M_{\odot}$ ; Fox et al. 2014; Richter 2017). We also compare our result with extragalactic CGM studies and find that our derived mass of the MW's CGM ( $M_{\text{gas,all}}$ ) is between the estimate from the COS-Halos team (Werk et al. 2014; Prochaska et al. 2017) and that of M31's CGM by Lehner et al. (2017). Prochaska et al. (2017) found the total mass of the cool, photoionized CGM of  $L \sim L^*$  galaxies at redshift  $\sim 0.2$  is  $(9.2 \pm 4.3) \times 10^{10} M_{\odot} (\frac{R}{160 \text{ kpc}})^2$ , which is  $(2.0 \pm 0.9) \times 10^{10} M_{\odot} (\frac{R}{75 \text{ kpc}})^2$  for our assumed volume. On the other hand, Lehner et al. (2017) derived a total gas mass of  $2 \times 10^8 M_{\odot} (\frac{R}{50 \text{ kpc}})^2 (\frac{Z}{Z_{\odot}})^{-1}$  for M31's CGM by considering Si II, Si III, and Si IV simultaneously within 50 kpc of the galaxy. This corresponds to a total gas mass of  $\sim 1.5 \times 10^9 M_{\odot} (\frac{R}{75 \text{ kpc}})^2 (\frac{Z}{0.3 Z_{\odot}})^{-1}$  adopting our assumed volume and metallicity for the MW's CGM.

We note that other methods, such as the shell-geometry and volume-filling factor, are also used to calculate CGM masses. For example, Werk et al. (2014) computed the CGM mass for COS-Halos galaxies by integrating the gas surface-density profile in an annular manner (see also Tumlinson et al. 2011; Bordoloi et al. 2014; Stern et al. 2016; Prochaska et al. 2017; etc.). If we apply this method and assume the Si IV-bearing gas is distributed over a spherical shell with radius of 75 kpc, the mass estimate for the cool gas in the MW CGM will be a factor of three higher. On the other hand, Stocke et al. (2013) estimated the CGM mass of late-type galaxies with a volume filling factor of 3%–5%. Briefly, they determined the volume-filling factor of warm CGM clouds by taking into account the covering fraction, the average number of ion absorption components along the sightlines, and the physical cloud sizes as inferred from photoionization modelings (see their equation 5). The total CGM mass was derived by summing up the mass of all available clouds with the assumption that warm clouds represent the whole CGM cloud population. Werk et al. (2014) calculated the CGM mass for the COS-Halos sample with both the surface-density method (as mentioned above) and the volume-filling method. With a volume-filling factor of 11%, they found consistent CGM mass results between the two methods. The volume-filling method has two requirements: (1) an estimate of cloud sizes based on CLOUDY modeling, and (2) an estimate of the average number of ion absorption components along the sightlines based on Voigt-profile fitting. Because neither of these is used in this work, we are unable to conduct mass estimate with the volume-filling method.

## 6. CONCLUSION

For MW absorption-line studies that rely on background QSOs, the LOSs unavoidably intercept the ISM, the disk-halo interface, and the CGM of the MW. Therefore, every QSO spectrum contains mixed absorption-line features from these sources. High-velocity gas ( $|v_{\text{LSR}}| > 100 \text{ km s}^{-1}$ ) is traditionally assumed to relate to the CGM, whereas low-intermediate velocity gas ( $|v_{\text{LSR}}| \leq 100 \text{ km s}^{-1}$ ) is considered to be more nearby. In this work, we study the all-sky distribution and origins of the Si IV-bearing gas at low-intermediate velocity with coadded G130M COS spectra of 132 QSOs obtained from HSLA DR1 (Peeples et al. 2017). Our results are summarized as follows.

First, the low-intermediate velocity Si IV measured toward all-sky QSOs has an average column density of  $\langle N \rangle = (3.8 \pm 1.4) \times 10^{13} \text{ cm}^{-2}$  (i.e.,  $\log N = 13.58 \pm 1.16$  dex). The Si IV column density does not significantly correlate with the Galactic latitude or longitude (see § 3). We find that most sightlines in the north show gas moving at negative velocities toward the LSR at  $-50 \lesssim v \lesssim 0 \text{ km s}^{-1}$ , which implies potential inflow. Sightlines in the south do not show such velocity preference.

Second, we examine our QSO data using a commonly adopted plane-parallel flat-slab model, but find that the flat-slab model cannot explain the  $\log N$  distribution as a function of  $b$  (see § 4.1). The flat slab predicts higher column densities at lower Galactic latitudes because the LOS paths going through the slab are longer; however, as summarized in the previous point, our data do not show such  $b$ -dependent trend.

Third, we propose a two-component model that consists of a disk-halo and a global component (see § 4.2). The disk-halo component  $N_{\text{DH}}^{\perp}$  is assumed to follow the flat-slab geometry; thus the LOS column-density scales with  $1/|\sin|b||$ . The global component  $N_{\text{G}}$  represents a general background that contributes identically from sightline to sightline. Additionally, we consider a patchiness parameter drawn from a Gaussian distribution  $(0, \sigma_p^2)$  to account for the intrinsic column density from sightline to sightline. We conduct Bayesian analyses and block bootstrapping to solve for  $(N_{\text{DH}}^{\perp}, N_{\text{G}}, \sigma_p)$ , and find  $N_{\text{DH}}^{\perp} = 1.3_{-0.7}^{+4.7} \times 10^{12} \text{ cm}^{-2}$ ,  $N_{\text{G}} = 3.4_{-0.3}^{+0.3} \times 10^{13} \text{ cm}^{-2}$ , and  $\sigma_p = 1.4 \times 10^{13} \text{ cm}^{-2}$ , which are consistent with the statistics measured from the data. Our two-component model is able to reproduce the column-density distribution seen toward distant QSOs (Figure 10).

Ultimately, we examine the origin(s) of the global component (§ 5.2) and find that it is most likely to be associated with the MW's CGM, although its exact location is difficult to constrain without distance measurements. If it were related to the MW's CGM, we would find a total mass of  $M_{\text{gas,all}} \gtrsim 4.7 \times 10^9 M_{\odot} (\frac{C_{\text{I}}}{1}) (\frac{R}{75 \text{ kpc}})^2 (\frac{f_{\text{SiIV}}}{0.3})^{-1} (\frac{Z}{0.3 Z_{\odot}})^{-1}$  for gas at cool

phases, including the mass of low-intermediate velocity gas ( $|v_{\text{LSR}}| \leq 100 \text{ km s}^{-1}$ ) directly probed in this work and that of the high-velocity gas ( $|v_{\text{LSR}}| > 100 \text{ km s}^{-1}$ ) inferred from a synthetic observation of a simulated MW-mass galaxy. Our mass estimates are consistent with MW ionized HVC studies and extragalactic CGM studies. This work shows that there is likely to be a considerable amount of ionized gas moving at low-intermediate velocity hidden in the MW's CGM.

In conducting this study, we perform continuum normalization for a total of 401 QSO spectra observed with HST/COS (§ 2.1), which is based on a QSO subset of HSLA DR1 (Peeples et al. 2017). Each coadded spectrum has G130M and/or G160M gratings and has a S/N  $\geq 5.0$  per resolution element over the wavelength span. Our continuum normalization focuses on Galactic interstellar absorption lines, including Fe II 1142/1143/1144/1608 Å, P II 1152 Å, S II 1250/1253/1259 Å, Si II 1190/1193/1260/1526 Å, Si III 1206 Å, Si IV 1393/1402 Å, C II 1334 Å, and C IV 1548/1550 Å. For each QSO we also retrieve H I 21cm emission lines from three H I surveys: GALFA-H I (Peek et al. 2018), LAB (Kalberla et al. 2005), and HI4PI (HI4PI Collaboration et al. 2016). The QSO continua, individual line spectra, and the corresponding H I 21cm lines together form our COS-GAL dataset, which we release to the public at [10.17909/T9N677]. In addition, the codes and data used in this work can be found at [https://github.com/yzhenggit/Zheng18\\_MWCGM](https://github.com/yzhenggit/Zheng18_MWCGM).

Critical information is missing when relying on QSOs to probe the MW halo – the distance. As we mention in § 5.1, ideally the stellar sample and the QSO sample should be combined to yield better constraints on the location to the Si IV content associated with the MW's disk-halo interface, thus shedding light on the distribution of the low-intermediate velocity gas hidden in the MW's CGM. The COS-GAL dataset can be further used to conduct preliminary studies of other interstellar lines related to the MW's ISM and halo components, such as studying the global phenomena of ionized HVCs, gas flows in different directions, the ionized gas properties in specific regions of the MW, or the surroundings of galaxies in the Local Group.

*Acknowledgement.* We thank the anonymous referees for their patient and useful comments in improving this manuscript. We are very grateful to B. Wakker and B. Savage for pointing out a critical systemic error in calculating the Si IV apparent column density in the first version. We thank K. Tchernyshyov, M. Peeples, S. Flemming, H.W. Chen, A. Fox, and Z.J. Qu for useful discussions on many parts of this manuscript. Y.Z. is partially supported by the Miller Institute for Basic Research in Science as of finishing this manuscript. JW acknowledges support from a 2018 Alfred P. Sloan Re-

search Fellowship. We acknowledge support from HST-GO-13706, HST-GO-13383, and HST-GO-13382 which were provided by NASA through grants from the Space Telescope Science Institute (STScI). STScI is operated by the Association of Universities for Research in Astronomy, Inc., under NASA contract NAS5-26555. Most of the data presented in this paper were obtained from the Mikulski Archive for Space Telescopes (MAST). We also acknowledge support from the National Science Foundation under Grant No. AST-1410800 and AST-1312888.

*Software:* Astropy (Astropy Collaboration et al. 2013), Linetools (Prochaska et al. 2016), IPython package (Pérez & Granger 2007), matplotlib (Hunter 2007), Emcee (Foreman-Mackey et al. 2013), Github.

## REFERENCES

- Ackermann, M., Albert, A., Atwood, W. B., et al. 2014, ApJ, 793, 64
- Albert, C. E., & Danly, L. 2004, in *Astrophysics and Space Science Library*, Vol. 312, High Velocity Clouds, ed. H. van Woerden, B. P. Wakker, U. J. Schwarz, & K. S. de Boer, 73
- Asplund, M., Grevesse, N., Sauval, A. J., & Scott, P. 2009, ARA&A, 47, 481
- Astropy Collaboration, Robitaille, T. P., Tollerud, E. J., et al. 2013, A&A, 558, A33
- Behroozi, P. S., Conroy, C., & Wechsler, R. H. 2010, ApJ, 717, 379
- Bordoloi, R., Prochaska, J. X., Tumlinson, J., et al. 2018, ApJ, 864, 132
- Bordoloi, R., Tumlinson, J., Werk, J. K., et al. 2014, ApJ, 796, 136
- Bordoloi, R., Fox, A. J., Lockman, F. J., et al. 2017, ApJ, 834, 191
- Bowen, D. V., Jenkins, E. B., Tripp, T. M., et al. 2008, ApJS, 176, 59
- Bregman, J. N., & Lloyd-Davies, E. J. 2007, ApJ, 669, 990
- Burchett, J. N., Tripp, T. M., Bordoloi, R., et al. 2016, ApJ, 832, 124
- Cen, R., & Ostriker, J. P. 1999, ApJ, 514, 1
- Collins, J. A., Shull, J. M., & Giroux, M. L. 2009, ApJ, 705, 962
- Danforth, C. W., Keeney, B. A., Stocke, J. T., Shull, J. M., & Yao, Y. 2010, ApJ, 720, 976
- Ferland, G. J., Korista, K. T., Verner, D. A., et al. 1998, PASP, 110, 761
- Ferland, G. J., Porter, R. L., van Hoof, P. A. M., et al. 2013, Rev. Mexicana Astron. Astrofis., 49, 137
- Foreman-Mackey, D. 2016, The Journal of Open Source Software, 24, doi:10.21105/joss.00024
- Foreman-Mackey, D., Hogg, D. W., Lang, D., & Goodman, J. 2013, PASP, 125, 306
- Fox, A. J., Savage, B. D., & Wakker, B. P. 2006, ApJS, 165, 229
- Fox, A. J., Wakker, B. P., Savage, B. D., et al. 2005, ApJ, 630, 332
- Fox, A. J., Wakker, B. P., Barger, K. A., et al. 2014, ApJ, 787, 147
- Fox, A. J., Bordoloi, R., Savage, B. D., et al. 2015, ApJL, 799, L7
- Fukugita, M., Hogan, C. J., & Peebles, P. J. E. 1998, ApJ, 503, 518
- Goodman, J., & Weare, J. 2010, Communications in Applied Mathematics and Computational Science, Vol. 5, No. 1, p. 65-80, 2010, 5, 65

- Haardt, F., & Madau, P. 2001, in *Clusters of Galaxies and the High Redshift Universe Observed in X-rays*, ed. D. M. Neumann & J. T. V. Tran, 64
- HI4PI Collaboration, Ben Bekhti, N., Flöer, L., et al. 2016, *A&A*, 594, A116
- Hogg, D. W., Bovy, J., & Lang, D. 2010, *ArXiv e-prints*, arXiv:1008.4686
- Hunter, J. D. 2007, *Computing In Science & Engineering*, 9, 90
- Ivezić, Ž., Connelly, A. J., VanderPlas, J. T., & Gray, A. 2014, *Statistics, Data Mining, and Machine Learning in Astronomy*
- Jenkins, E. B. 1978, *ApJ*, 219, 845
- Joung, M. R., Putman, M. E., Bryan, G. L., Fernández, X., & Peek, J. E. G. 2012, *ApJ*, 759, 137
- Kalberla, P. M. W., Burton, W. B., Hartmann, D., et al. 2005, *A&A*, 440, 775
- Keeney, B. A., Danforth, C. W., Stocke, J. T., France, K., & Green, J. C. 2012, *PASP*, 124, 830
- Keeney, B. A., Stocke, J. T., Danforth, C. W., et al. 2017, *ApJS*, 230, 6
- Lehner, N., & Howk, J. C. 2007, *MNRAS*, 377, 687
- Lehner, N., Howk, J. C., Thom, C., et al. 2012, *MNRAS*, 424, 2896
- Lehner, N., Howk, J. C., & Wakker, B. P. 2015, *ApJ*, 804, 79
- , 2017, *ApJ*, 848, 71
- Liang, C. J., & Chen, H.-W. 2014, *MNRAS*, 445, 2061
- Marasco, A., Fraternali, F., & Binney, J. J. 2012, *MNRAS*, 419, 1107
- Morton, D. C. 2003, *ApJS*, 149, 205
- Nicastro, F., Zezas, A., Elvis, M., et al. 2003, *Nature*, 421, 719
- Nidever, D. L., Majewski, S. R., Butler Burton, W., & Nigra, L. 2010, *ApJ*, 723, 1618
- Peek, J. E. G., Heiles, C., Putman, M. E., & Douglas, K. 2009, *ApJ*, 692, 827
- Peek, J. E. G., Babler, B. L., Zheng, Y., et al. 2018, *ApJS*, 234, 2
- Peebles, M., Tumlinson, J., Fox, A., et al. 2017, *The Hubble Spectroscopic Legacy Archive*, Tech. rep.
- Peebles, M. S., & Shankar, F. 2011, *MNRAS*, 417, 2962
- Pérez, F., & Granger, B. E. 2007, *Computing in Science and Engineering*, 9, 21
- Persic, M., & Salucci, P. 1992, *MNRAS*, 258, 14P
- Planck Collaboration, Ade, P. A. R., Aghanim, N., et al. 2016, *A&A*, 594, A25
- Prochaska, J. X., Tejos, N., Crighton, N., Burchett, J., & Tuo-Ji. 2016, *linetools/linetools: Second major release, v.v0.2*, Zenodo, doi:10.5281/zenodo.168270
- Prochaska, J. X., Werk, J. K., Worseck, G., et al. 2017, *ApJ*, 837, 169
- Putman, M. E., Peek, J. E. G., & Joung, M. R. 2012, *ARA&A*, 50, 491
- Rafelski, M., & et al. 2018, *COS Data Handbook v. 4.0*
- Richter, P. 2017, in *Astrophysics and Space Science Library*, Vol. 430, *Gas Accretion onto Galaxies*, ed. A. Fox & R. Davé, 15
- Rubin, K. H. R., Prochaska, J. X., Koo, D. C., et al. 2014, *ApJ*, 794, 156
- Saul, D. R., Peek, J. E. G., & Putman, M. E. 2014, *MNRAS*, 441, 2266
- Savage, B. D., Edgar, R. J., & Diplas, A. 1990, *ApJ*, 361, 107
- Savage, B. D., & Lehner, N. 2006, *ApJS*, 162, 134
- Savage, B. D., & Sembach, K. R. 1991, *ApJ*, 379, 245
- , 1996, *ARA&A*, 34, 279
- Savage, B. D., & Wakker, B. P. 2009, *ApJ*, 702, 1472
- Savage, B. D., Sembach, K. R., Wakker, B. P., et al. 2003, *ApJS*, 146, 125
- Schwarz, U. J., & de Boer, K. S. 2004, in *Astrophysics and Space Science Library*, Vol. 312, *High Velocity Clouds*, ed. H. van Woerden, B. P. Wakker, U. J. Schwarz, & K. S. de Boer, 55
- Sembach, K. R., Wakker, B. P., Savage, B. D., et al. 2003, *ApJS*, 146, 165
- Shapiro, P. R., & Field, G. B. 1976, *ApJ*, 205, 762
- Shull, J. M. 2014, *ApJ*, 784, 142
- Shull, J. M., Jones, J. R., Danforth, C. W., & Collins, J. A. 2009, *ApJ*, 699, 754
- Stern, J., Hennawi, J. F., Prochaska, J. X., & Werk, J. K. 2016, *ApJ*, 830, 87
- Stocke, J. T., Keeney, B. A., Danforth, C. W., et al. 2013, *ApJ*, 763, 148
- Tumlinson, J., Thom, C., Werk, J. K., et al. 2011, *Science*, 334, 948
- , 2013, *ApJ*, 777, 59
- van Woerden, H., Wakker, B. P., Schwarz, U. J., & de Boer, K. S., eds. 2004, *Astrophysics and Space Science Library*, Vol. 312, *High Velocity Clouds*
- Wakker, B. P. 1991, in *IAU Symposium*, Vol. 144, *The Interstellar Disk-Halo Connection in Galaxies*, ed. H. Bloemen, 27–40
- Wakker, B. P. 2004, in *Astrophysics and Space Science Library*, Vol. 312, *High Velocity Clouds*, ed. H. van Woerden, B. P. Wakker, U. J. Schwarz, & K. S. de Boer, 25
- Wakker, B. P., Hernandez, A. K., French, D. M., et al. 2015, *ApJ*, 814, 40
- Wakker, B. P., Kalberla, P. M. W., van Woerden, H., de Boer, K. S., & Putman, M. E. 2001, *ApJS*, 136, 537
- Wakker, B. P., Savage, B. D., Fox, A. J., Benjamin, R. A., & Shapiro, P. R. 2012, *ApJ*, 749, 157
- Werk, J. K., Prochaska, J. X., Thom, C., et al. 2013, *ApJS*, 204, 17
- Werk, J. K., Prochaska, J. X., Tumlinson, J., et al. 2014, *ApJ*, 792, 8
- Werk, J. K., Prochaska, J. X., Cantalupo, S., et al. 2016, *ApJ*, 833, 54
- Zahedy, F. S., Chen, H.-W., Johnson, S. D., et al. 2018, *ArXiv e-prints*, arXiv:1809.05115
- Zheng, Y., Peek, J. E. G., Werk, J. K., & Putman, M. E. 2017, *ApJ*, 834, 179
- Zheng, Y., Putman, M. E., Peek, J. E. G., & Joung, M. R. 2015, *ApJ*, 807, 103

Table 1: Si IV Data Sample

No.	HSLA-ID	Glon ( $^{\circ}$ )	Glat ( $^{\circ}$ )	$z$	S/N	$Q$	$\log N_{1393}$	$v_{c,1393}$ ( $\text{km s}^{-1}$ )	$\log N_{1402}$	$v_{c,1402}$ ( $\text{km s}^{-1}$ )	Simbad ID
(0)	(1)	(2)	(3)	(4)	(5)	(6)	(7)	(8)	(9)	(10)	(11)
1	NGC-5548	31.9607	70.4957	0.0163	154.2	0	13.75 $\pm$ 0.00	-43.8 $\pm$ 0.3	13.75 $\pm$ 0.00	-45.2 $\pm$ 0.5	NGC 5548
2	MARK509	35.9711	-29.8553	0.0341	92.8	0	13.83 $\pm$ 0.00	22.6 $\pm$ 0.3	13.83 $\pm$ 0.00	26.6 $\pm$ 0.6	Mrk 509
3	MRK876	98.2694	40.3758	0.1385	84.9	0	13.64 $\pm$ 0.00	-24.6 $\pm$ 0.5	13.64 $\pm$ 0.01	-20.5 $\pm$ 1.0	Mrk 876
4	RXJ1230.8+0115	291.2605	63.6602	0.1170	61.6	0	13.53 $\pm$ 0.01	-5.8 $\pm$ 0.8	13.54 $\pm$ 0.01	-4.3 $\pm$ 1.6	2MASS J12305003+0115226
5	PG0804+761	138.2787	31.0327	0.1000	59.7	0	13.58 $\pm$ 0.01	-37.3 $\pm$ 0.9	13.60 $\pm$ 0.01	-35.7 $\pm$ 1.8	2MAXI J0808+757
6	NGC-7469	83.0985	-45.4670	0.0159	58.4	0	13.50 $\pm$ 0.01	-0.8 $\pm$ 0.9	13.50 $\pm$ 0.01	-2.6 $\pm$ 1.7	NGC 7469
7	PG1116+215	223.3600	68.2094	0.1765	47.4	0	13.68 $\pm$ 0.01	-12.9 $\pm$ 0.9	13.69 $\pm$ 0.01	-11.2 $\pm$ 1.4	Ton 1388
8	IRAS-F22456-5125	338.5115	-56.6293	0.1000	47.3	0	13.33 $\pm$ 0.01	6.9 $\pm$ 1.6	13.34 $\pm$ 0.03	8.4 $\pm$ 3.2	2MASS J22484115-5109532
9	PKS2155-304	17.7305	-52.2458	0.1160	45.7	0	13.38 $\pm$ 0.01	0.3 $\pm$ 1.5	13.36 $\pm$ 0.02	-1.6 $\pm$ 3.1	QSO B2155-304
10	PG1352+183	4.3748	72.8738	0.1515	44.5	0	13.65 $\pm$ 0.01	-34.2 $\pm$ 1.3	13.64 $\pm$ 0.02	-39.5 $\pm$ 2.4	2E 1352.2+1820
11	IO-AND	122.2786	-23.1812	0.1340	43.0	0	13.26 $\pm$ 0.02	-28.5 $\pm$ 2.2	13.26 $\pm$ 0.03	-10.0 $\pm$ 4.1	2MASX J00481899+3941118
12	MRK817	100.2997	53.4783	0.0315	42.9	0	13.47 $\pm$ 0.01	-33.2 $\pm$ 1.6	13.48 $\pm$ 0.02	-30.0 $\pm$ 2.9	Mrk 817
13	IRAS-L06229-6434	274.3116	-27.3194	0.1290	42.4	0	13.35 $\pm$ 0.01	12.7 $\pm$ 1.9	13.33 $\pm$ 0.03	23.6 $\pm$ 4.1	[VV98] J062309.1-643624
14	TONS210	224.9716	-83.1603	0.1160	42.0	0	13.63 $\pm$ 0.01	-15.7 $\pm$ 1.0	13.64 $\pm$ 0.02	-14.5 $\pm$ 2.0	Ton S 210
15	NGC-985	180.8371	-59.4903	0.0427	40.6	0	13.35 $\pm$ 0.01	-39.1 $\pm$ 2.2	13.36 $\pm$ 0.03	-31.4 $\pm$ 4.0	NGC 985
16	PG0052+251	123.9075	-37.4377	0.1550	40.3	0	13.35 $\pm$ 0.02	-17.6 $\pm$ 2.1	13.37 $\pm$ 0.02	-19.0 $\pm$ 2.9	2E 217
17	PHL1811	47.4735	-44.8151	0.1940	39.6	0	13.61 $\pm$ 0.01	1.2 $\pm$ 1.0	13.60 $\pm$ 0.02	2.0 $\pm$ 2.0	QSO J2155-0922
18	PG-1407+265	34.6686	72.5886	0.9400	36.6	0	13.78 $\pm$ 0.01	-43.1 $\pm$ 1.3	13.77 $\pm$ 0.01	-39.1 $\pm$ 2.1	QSO J1409+2618
19	HE0226-4110	253.9406	-65.7747	0.4934	36.0	0	13.36 $\pm$ 0.02	-0.8 $\pm$ 2.0	13.36 $\pm$ 0.03	8.3 $\pm$ 4.0	HE 0226-4110
20	3C263	134.1590	49.7439	0.6520	35.8	0	13.70 $\pm$ 0.01	-44.7 $\pm$ 1.5	13.71 $\pm$ 0.02	-39.9 $\pm$ 2.4	7C 113710.40+660425.00
21	FAIRALL9	295.0729	-57.8265	0.0480	35.6	0	13.59 $\pm$ 0.01	12.9 $\pm$ 1.3	13.60 $\pm$ 0.02	20.9 $\pm$ 2.6	ESO 113-45
22	PG0953+414	179.7860	51.7091	0.2341	35.4	0	13.38 $\pm$ 0.02	-21.8 $\pm$ 2.1	13.41 $\pm$ 0.03	-13.2 $\pm$ 3.8	2XMM J095652.4+411522
23	QSO-B1307+085	316.7864	70.7068	0.1543	35.2	0	13.73 $\pm$ 0.01	-21.5 $\pm$ 1.2	13.71 $\pm$ 0.01	-21.2 $\pm$ 1.6	2E 2978
24	PG1259+593	120.5554	58.0479	0.4778	34.7	0	13.36 $\pm$ 0.02	-18.1 $\pm$ 2.2	13.37 $\pm$ 0.03	-10.6 $\pm$ 4.3	LB 2522
25	HE0056-3622	293.7190	-80.8980	0.1641	34.4	0	13.63 $\pm$ 0.01	-9.4 $\pm$ 1.3	13.64 $\pm$ 0.02	-3.0 $\pm$ 2.0	6dFGS gJ005837.4-360605
26	VIIZW244	136.6575	32.6778	0.1313	34.1	0	13.59 $\pm$ 0.01	-45.7 $\pm$ 1.9	13.61 $\pm$ 0.02	-35.4 $\pm$ 2.9	MCG+13-07-002
27	IES1553+113	21.9089	43.9642	0.3600	34.0	0	13.96 $\pm$ 0.01	-3.5 $\pm$ 0.6	13.95 $\pm$ 0.01	-7.6 $\pm$ 1.1	QSO B1553+113
28	ESO-141-55	338.1834	-26.7112	0.0370	33.4	0	13.80 $\pm$ 0.01	4.2 $\pm$ 0.9	13.81 $\pm$ 0.01	4.2 $\pm$ 1.6	ESO 141-55
29	S50716+714	143.9811	28.0176	0.3000	33.4	0	13.47 $\pm$ 0.01	-34.8 $\pm$ 2.1	13.45 $\pm$ 0.03	-42.3 $\pm$ 4.5	7C 071610.69+712601.00
30	PG1626+554	84.5149	42.1886	0.1330	33.2	0	13.53 $\pm$ 0.01	-24.1 $\pm$ 1.7	13.55 $\pm$ 0.02	-24.1 $\pm$ 3.1	QSO B1626+5529

Note - Col (0): QSOs are arranged from high to low S/N per resolution element. Col (1): QSO ID as adopted by HSLA first data release (Peeples et al. 2017). Col (2) and (3): Galactic longitude and latitude as provided on Simbad. Col (4): QSO redshift as provided on Simbad. Col (5): S/N per resolution element for the absorption-free region between 1394Å and 1401Å. The S/N value can be calculated as  $S/N \text{ per pix} \times N/\sqrt{N}$ , where  $N$  is the total number of pixels for a corresponding resolution. For G130M grating,  $N = 6$ . Col (6): Quality flagging (see § 2.2):  $Q = 0$  means this target has spectrally resolved doublet profiles,  $Q = 1$  means its Si IV lines are saturated, and  $Q = -1$  means its 1393 Å line is abnormally stronger than 1402 Å. Col (7) and (8): logarithmic apparent column density and centroid velocity for Si IV 1393Å integrated from -100 to 100  $\text{km s}^{-1}$ . Col (9) and (10): Same as Col (7) and (8), but for Si IV 1402 Å. Col (11): Simbad ID. The machine readable version of this table can be downloaded here: [https://github.com/yzhenggit/Zheng18\\_MWCGM/](https://github.com/yzhenggit/Zheng18_MWCGM/).

Table 1 continued

No.	HSLA-ID	Glom ( $^{\circ}$ ) (2)	Glat ( $^{\circ}$ ) (3)	$z$	S/N	$Q$	$\log N_{\text{H}1393}$	$v_{c,1393}$ ( $\text{km s}^{-1}$ ) (8)	$\log N_{\text{H}1402}$	$v_{c,1402}$ ( $\text{km s}^{-1}$ ) (10)	Simbad ID
(0)	(1)	(2)	(3)	(4)	(5)	(6)	(7)	(8)	(9)	(10)	(11)
31	MR2251-178	46.1973	-61.3256	0.0640	32.8	0	13.65 $\pm$ 0.01	9.9 $\pm$ 1.1	13.65 $\pm$ 0.02	13.5 $\pm$ 2.4	NAME MR 2251-178
32	SDSSJ135341.03+361948.0	71.6687	73.9144	0.1470	32.2	0	13.36 $\pm$ 0.02	-39.1 $\pm$ 2.5	13.37 $\pm$ 0.04	-44.6 $\pm$ 6.9	2MASS J13534104+3619480
33	LBQS-1435-0134	348.7185	51.3746	1.3077	31.1	0	13.75 $\pm$ 0.01	-21.4 $\pm$ 1.2	13.76 $\pm$ 0.02	-19.9 $\pm$ 2.0	LBQS 1435-0134
34	IRASF00040+4325	114.4161	-18.4214	0.1660	31.0	0	13.20 $\pm$ 0.03	-29.5 $\pm$ 4.0	13.21 $\pm$ 0.04	-22.5 $\pm$ 6.3	IRAS 00040+4325
35	MRK-335	108.7635	-41.4244	0.0250	31.0	0	13.59 $\pm$ 0.01	-9.1 $\pm$ 1.4	13.61 $\pm$ 0.02	-6.6 $\pm$ 2.6	Mrk 335
36	NGC-3783	287.4560	-22.9474	0.0098	30.8	0	13.75 $\pm$ 0.01	11.1 $\pm$ 1.1	13.76 $\pm$ 0.01	9.8 $\pm$ 1.8	NGC 3783
37	1H-2129-624	331.1427	-42.5233	0.0590	30.3	0	13.65 $\pm$ 0.01	29.0 $\pm$ 1.5	13.66 $\pm$ 0.02	29.7 $\pm$ 2.8	2MAXI J2136-624
38	MRK106	161.1389	42.8794	0.1228	30.2	0	13.31 $\pm$ 0.02	-21.5 $\pm$ 2.8	13.33 $\pm$ 0.04	-20.6 $\pm$ 6.0	Mrk 106
39	RXS-J23218-7026	313.2923	-44.8373	0.3000	29.4	0	13.63 $\pm$ 0.01	19.2 $\pm$ 1.5	13.65 $\pm$ 0.02	26.8 $\pm$ 2.9	2MASS J23215113-7026441
40	PKS0552-640	273.4656	-30.6114	0.6840	28.8	0	13.42 $\pm$ 0.02	20.7 $\pm$ 2.4	13.46 $\pm$ 0.03	31.8 $\pm$ 4.6	2MASS J05522451-6402108
41	RXJ2154.1-4414	355.1794	-50.8647	0.3440	28.8	0	13.58 $\pm$ 0.01	22.2 $\pm$ 1.5	13.60 $\pm$ 0.03	28.5 $\pm$ 3.7	2MASS J21545109-4414057
42	HE0238-1904	200.4807	-63.6334	0.6280	27.0	0	13.47 $\pm$ 0.02	-11.7 $\pm$ 2.2	13.50 $\pm$ 0.03	0.0 $\pm$ 3.8	QSO B0238-1904
43	MRK1513	63.6697	-29.0695	0.0620	26.8	0	13.73 $\pm$ 0.01	2.9 $\pm$ 1.2	13.74 $\pm$ 0.02	9.6 $\pm$ 2.3	Mrk 1513
44	B0117-2837	225.7305	-83.6507	0.3490	26.4	0	13.63 $\pm$ 0.01	-7.0 $\pm$ 1.5	13.64 $\pm$ 0.03	-6.7 $\pm$ 3.5	2E 357
45	QSO-B0026+129	114.6377	-49.2459	0.1420	26.4	0	13.41 $\pm$ 0.01	-16.1 $\pm$ 1.9	13.44 $\pm$ 0.04	-6.8 $\pm$ 5.5	2E 93
46	PG1126-041	267.6305	52.7454	0.0600	26.1	0	13.43 $\pm$ 0.02	11.2 $\pm$ 2.4	13.46 $\pm$ 0.03	20.3 $\pm$ 4.6	Mrk 1298
47	PG1011-040	246.5010	40.7487	0.0580	25.9	0	13.37 $\pm$ 0.02	11.2 $\pm$ 2.8	13.41 $\pm$ 0.04	13.9 $\pm$ 5.1	QSO B1011-040
48	HE0153-4520	271.7954	-67.9751	0.4510	25.8	0	13.42 $\pm$ 0.02	4.1 $\pm$ 2.4	13.45 $\pm$ 0.04	-7.0 $\pm$ 4.5	[VV2000] J015513.2-450612
49	2XMM-J141348.3+440014	83.8280	66.3534	0.0870	25.5	0	13.44 $\pm$ 0.02	-45.5 $\pm$ 3.3	13.44 $\pm$ 0.04	-29.6 $\pm$ 5.7	2MASS J14134834+4400141
50	HE2347-4342	336.0339	-69.5737	2.8850	25.0	0	13.54 $\pm$ 0.02	-10.9 $\pm$ 2.2	13.56 $\pm$ 0.03	-5.1 $\pm$ 4.0	QSO B2347-4342
51	RXSJ09565-0452	243.3318	37.0043	0.1570	24.8	0	13.67 $\pm$ 0.01	13.1 $\pm$ 1.8	13.67 $\pm$ 0.02	14.6 $\pm$ 2.6	2MASX J09563012-0453174
52	MRK304	75.9893	-34.2225	0.0663	24.8	0	13.82 $\pm$ 0.01	-9.0 $\pm$ 1.1	13.83 $\pm$ 0.02	-7.0 $\pm$ 2.1	Mrk 304
53	PG1048+342	190.6025	63.4374	0.1671	24.6	0	13.70 $\pm$ 0.01	-24.9 $\pm$ 1.8	13.70 $\pm$ 0.02	-19.6 $\pm$ 2.6	QSO B1048+342
54	RXSJ00537+2232	123.6380	-40.3290	0.1464	24.6	0	13.38 $\pm$ 0.02	-18.9 $\pm$ 2.8	13.41 $\pm$ 0.06	-22.0 $\pm$ 7.9	2MASX J00534617+2232222
55	3C-66A	140.1429	-16.7669	0.3400	24.5	0	13.31 $\pm$ 0.03	-21.9 $\pm$ 3.6	13.31 $\pm$ 0.05	-38.2 $\pm$ 7.9	7C 021929.69+424830.00
56	NGC-4051	148.8832	70.0852	0.0022	24.5	0	13.67 $\pm$ 0.02	-20.6 $\pm$ 2.0	13.65 $\pm$ 0.02	-22.7 $\pm$ 3.3	NGC 4051
57	3C57	173.0775	-67.2618	0.6710	24.4	0	13.39 $\pm$ 0.02	-17.5 $\pm$ 2.9	13.41 $\pm$ 0.04	-21.7 $\pm$ 5.7	2MASS J02015718-1132334
58	PG0003+158	107.3184	-45.3258	0.4505	24.4	0	13.51 $\pm$ 0.02	7.4 $\pm$ 2.2	13.53 $\pm$ 0.03	-2.6 $\pm$ 4.1	2E 12
59	MRK1392	2.7540	50.2640	0.0359	24.2	0	13.71 $\pm$ 0.01	-22.7 $\pm$ 1.6	13.73 $\pm$ 0.02	-24.1 $\pm$ 2.8	Mrk 1392
60	RXS-J00057-5007	320.7098	-65.4054	0.0333	24.1	0	13.69 $\pm$ 0.01	3.1 $\pm$ 1.5	13.70 $\pm$ 0.02	6.1 $\pm$ 2.9	2EUVE J0005-50.0
61	PG1216+069	281.0714	68.1432	0.3313	22.9	0	13.51 $\pm$ 0.02	-12.0 $\pm$ 2.2	13.52 $\pm$ 0.04	-3.8 $\pm$ 4.5	PG 1216+069
62	4C-01.61	91.6647	-60.3620	0.1740	22.6	0	13.38 $\pm$ 0.02	1.5 $\pm$ 3.0	13.37 $\pm$ 0.04	2.0 $\pm$ 5.7	4C -01.61
63	QSO-B1215+303	188.8752	82.0529	0.2370	22.2	0	13.34 $\pm$ 0.03	-29.0 $\pm$ 3.8	13.38 $\pm$ 0.05	-21.8 $\pm$ 6.6	7C 121521.39+302340.00
64	HE2258-5524	330.7246	-55.6698	0.1400	21.8	0	13.36 $\pm$ 0.03	8.1 $\pm$ 3.2	13.39 $\pm$ 0.05	12.5 $\pm$ 6.3	6dFGS gJ230152.0-550831
65	IZW1	123.7486	-50.1750	0.0600	21.4	0	13.40 $\pm$ 0.02	-17.0 $\pm$ 3.2	13.42 $\pm$ 0.05	-22.5 $\pm$ 6.4	Mrk 1502

Table 1 continued

No.	HSLA-ID	Glon ( $^{\circ}$ )	Glat ( $^{\circ}$ )	$z$	S/N	$Q$	$\log N_{1393}$	$v_{e,1393}$ ( $\text{km s}^{-1}$ )	$\log N_{1402}$	$v_{e,1402}$ ( $\text{km s}^{-1}$ )	Simbad ID
(0)	(1)	(2)	(3)	(4)	(5)	(6)	(7)	(8)	(9)	(10)	(11)
66	SDSSJ232259.98-005359.2	80.2739	-56.2638	0.1505	21.4	0	13.45 $\pm$ 0.03	14.1 $\pm$ 3.5	13.49 $\pm$ 0.05	6.2 $\pm$ 6.1	2MASX J23230004-0053588
67	MRK290	91.4892	47.9534	0.0302	21.3	0	13.49 $\pm$ 0.02	-29.2 $\pm$ 3.0	13.50 $\pm$ 0.04	-18.6 $\pm$ 5.2	Mrk 290
68	RXS-121388-3828	4.5094	-48.4648	0.1830	20.9	0	13.64 $\pm$ 0.02	19.3 $\pm$ 2.2	13.62 $\pm$ 0.03	26.0 $\pm$ 4.2	2MASX J21384992-3828403
69	PG1222+216	255.0731	81.6598	0.4338	20.7	0	13.63 $\pm$ 0.02	-7.2 $\pm$ 2.0	13.66 $\pm$ 0.03	2.5 $\pm$ 3.6	4C 21-35
70	MRK-1044	179.6944	-60.4774	0.0161	20.6	0	13.45 $\pm$ 0.02	-30.9 $\pm$ 3.4	13.49 $\pm$ 0.04	-34.3 $\pm$ 6.2	Mrk 1044
71	Q0439-433	247.9801	-41.3828	0.5937	19.7	0	13.67 $\pm$ 0.02	-1.5 $\pm$ 1.9	13.69 $\pm$ 0.03	0.5 $\pm$ 3.5	QSO J0441-4313
72	2MASX-J10053271-2417161	261.2303	24.8511	0.1540	19.2	0	13.53 $\pm$ 0.04	29.5 $\pm$ 5.4	13.55 $\pm$ 0.03	36.6 $\pm$ 5.1	2MASX J10053271-2417161
73	QSO-B1440+3539	59.2376	65.0346	0.0770	18.8	0	13.52 $\pm$ 0.03	-51.4 $\pm$ 4.9	13.56 $\pm$ 0.04	-48.4 $\pm$ 6.5	Mrk 478
74	RBS144	299.4837	-65.8362	0.0628	18.7	0	13.49 $\pm$ 0.02	1.1 $\pm$ 2.9	13.51 $\pm$ 0.05	29.8 $\pm$ 6.5	2MASX J01002713-5113544
75	PG1112+431	167.8870	64.9397	0.3010	18.3	0	13.54 $\pm$ 0.02	-36.5 $\pm$ 3.6	13.54 $\pm$ 0.04	-41.6 $\pm$ 6.8	QSO B1112+4306
76	PG1001+291	200.0834	53.2070	0.3297	18.3	0	13.64 $\pm$ 0.02	-27.3 $\pm$ 3.0	13.64 $\pm$ 0.03	-27.6 $\pm$ 4.9	Ton 28
77	RBS2055	106.6724	-34.6586	0.0400	18.3	0	13.73 $\pm$ 0.02	-12.3 $\pm$ 1.9	13.76 $\pm$ 0.03	-10.1 $\pm$ 3.3	2MASX J23515277+2619325
78	QSO-B1617+1731	32.8943	41.0760	0.1120	18.2	0	13.82 $\pm$ 0.02	-22.7 $\pm$ 2.0	13.85 $\pm$ 0.03	-20.5 $\pm$ 3.3	Mrk 877
79	HS1831+5338	82.5864	24.2127	0.0450	18.2	0	13.69 $\pm$ 0.02	-24.1 $\pm$ 2.6	13.68 $\pm$ 0.03	-20.1 $\pm$ 4.4	2MASX J18324966+5340219
80	MRK1148	123.0934	-45.4387	0.0640	18.1	0	13.41 $\pm$ 0.03	-5.9 $\pm$ 3.5	13.46 $\pm$ 0.05	-18.3 $\pm$ 7.0	Mrk 1148
81	B0120-28	227.7753	-82.9332	0.4360	18.0	0	13.60 $\pm$ 0.02	-12.3 $\pm$ 2.8	13.64 $\pm$ 0.04	-3.1 $\pm$ 4.4	QSO B0120-28
82	NGC-3516	133.2357	42.4028	N/A	17.8	0	13.31 $\pm$ 0.04	-50.9 $\pm$ 7.1	13.36 $\pm$ 0.06	-50.5 $\pm$ 9.8	[MWP92] A
83	HS1102+3441	188.5631	66.2187	0.5083	17.7	0	13.68 $\pm$ 0.02	-24.3 $\pm$ 2.7	13.70 $\pm$ 0.03	-27.0 $\pm$ 4.4	Ton 1329
84	PG-1132+416	90.5870	72.4836	1.2144	17.7	0	13.41 $\pm$ 0.03	-41.8 $\pm$ 5.3	13.42 $\pm$ 0.06	-28.8 $\pm$ 8.5	QSO J1341+4123
85	TON236	44.4335	55.3506	0.4474	17.6	0	13.72 $\pm$ 0.02	-44.5 $\pm$ 3.9	13.70 $\pm$ 0.03	-36.4 $\pm$ 5.2	Ton 236
86	RBS1892	345.8980	-58.3672	0.1980	17.5	0	13.52 $\pm$ 0.03	-10.4 $\pm$ 3.2	13.56 $\pm$ 0.04	-2.4 $\pm$ 5.3	2MASS J22452029-4652116
87	HB89-0232-042	174.4627	-56.1555	1.4250	17.4	0	13.38 $\pm$ 0.03	-8.0 $\pm$ 4.1	13.41 $\pm$ 0.06	1.9 $\pm$ 7.8	[RKV2003] <sup>a</sup>
88	3C48	133.9626	-28.7195	0.3690	17.3	0	13.51 $\pm$ 0.03	-23.1 $\pm$ 3.7	13.48 $\pm$ 0.05	-13.2 $\pm$ 6.8	3C 48
89	RBS1666	358.7326	-31.0031	0.0796	17.2	0	13.89 $\pm$ 0.02	28.0 $\pm$ 2.4	13.89 $\pm$ 0.02	26.8 $\pm$ 3.3	6dFGS gJ200553.0-413442
90	2XMM-J100420.0+051300	234.1610	44.6222	0.1600	17.0	0	13.54 $\pm$ 0.03	6.4 $\pm$ 3.4	13.54 $\pm$ 0.05	8.7 $\pm$ 6.3	2MASS J10042013+0513004
91	PG1121+422	167.2578	66.8587	0.2249	16.9	0	13.60 $\pm$ 0.02	-38.9 $\pm$ 3.9	13.64 $\pm$ 0.04	-23.7 $\pm$ 5.4	2MASS J1124392+420144
92	SDSSJ094733.21+100508.7	225.3726	43.5395	0.1390	16.7	0	13.59 $\pm$ 0.02	-9.0 $\pm$ 2.7	13.60 $\pm$ 0.05	-21.6 $\pm$ 6.8	2MASX J09473320+1005093
93	RXSJ00437+3725	121.2330	-25.4241	0.0800	16.3	0	13.50 $\pm$ 0.03	-25.4 $\pm$ 4.1	13.51 $\pm$ 0.05	-31.8 $\pm$ 7.7	LEDA 2100384
94	ZW535.012	120.1743	-17.1260	0.0477	16.1	0	13.30 $\pm$ 0.05	-16.3 $\pm$ 5.9	13.30 $\pm$ 0.08	-20.0 $\pm$ 11.2	2MASX J00362092+4539532
95	RXJ0439.6-5311	261.2159	-40.9266	0.2430	16.0	0	13.48 $\pm$ 0.03	-5.9 $\pm$ 3.6	13.50 $\pm$ 0.06	-3.3 $\pm$ 7.0	[VV98] J043938.7-531131
96	SDSSJ141542.90+163413.8	8.8491	67.8261	0.7426	15.9	0	13.84 $\pm$ 0.02	-37.4 $\pm$ 3.1	13.86 $\pm$ 0.03	-35.0 $\pm$ 4.3	QSO J1415+1634
97	RBS2000	350.1951	-67.5844	0.1736	15.6	0	13.60 $\pm$ 0.03	-12.1 $\pm$ 3.1	13.63 $\pm$ 0.05	-17.3 $\pm$ 5.8	2FHL J2324.7-4041
98	PHL2525	80.6832	-71.3172	0.2000	15.4	0	13.68 $\pm$ 0.02	-19.7 $\pm$ 3.0	13.71 $\pm$ 0.04	-32.1 $\pm$ 5.5	GD 1332
99	RXSJ00508+3536	122.7965	-27.2597	0.0580	15.3	0	13.47 $\pm$ 0.03	-29.2 $\pm$ 4.8	13.46 $\pm$ 0.06	-25.2 $\pm$ 8.7	2MASX J00505076+3536430
100	SDSSJ110307.57+291230.0	201.5586	66.0912	0.3655	15.0	0	13.52 $\pm$ 0.04	-8.7 $\pm$ 3.9	13.50 $\pm$ 0.05	-14.4 $\pm$ 6.4	[VV96] J110307.6+291230

<sup>a</sup>[RKV2003] QSO J0235-0402 abs 1.425

Table 1 continued

No.	HSLA-ID	Gl <sub>lon</sub> ( <sup>∘</sup> ) (2)	Gl <sub>lat</sub> ( <sup>∘</sup> ) (3)	<i>z</i> (4)	S/N (5)	<i>Q</i> (6)	log $N_{1393}$ (7)	$v_{c,1393}$ (km s <sup>-1</sup> ) (8)	log $N_{1402}$ (9)	$v_{c,1402}$ (km s <sup>-1</sup> ) (10)	Simbad ID (11)
101	Q1545+210	33.8983	49.4574	0.2643	14.9	0	13.84±0.02	-24.3±2.7	13.86±0.03	-23.7±4.1	2MASX J15474353+2052167
102	CAL-F-COPY	277.1769	-35.4212	0.0640	14.8	0	13.52±0.03	14.1±4.0	13.54±0.06	14.7±7.4	6dFGS gJ050304.0-663346
103	TON1187	188.3286	55.3777	0.0789	14.8	0	13.48±0.03	-25.7±4.7	13.49±0.06	-20.5±7.9	Ton 1187
104	FBQSJ1010+3003	198.4272	54.6251	0.2560	14.7	0	13.61±0.03	-29.9±4.4	13.63±0.05	-34.8±7.0	Ton 488
105	Q0349-146	205.4845	-46.3250	0.6170	14.6	0	13.44±0.04	-13.2±4.5	13.49±0.06	-1.0±7.8	2MASS J03512857-1429082
106	PMNJ1103-2329	273.1898	33.0793	0.1860	14.5	0	13.36±0.04	37.3±7.2	13.41±0.07	24.5±11.0	2FHL J1104.0-2331
107	HB89-0107-025-NEID05	134.0294	-64.7793	0.9560	14.4	0	13.48±0.04	-14.9±4.5	13.49±0.07	-19.5±9.2	QSO J0110-0218
108	RBS563	272.2534	-39.2259	0.0690	14.2	0	13.23±0.05	-10.4±6.6	13.29±0.13	7.1±16.7	2MASX J04382919-6147587
109	HE2259-5524	330.6372	-55.7230	0.8510	14.2	0	13.46±0.04	10.2±4.6	13.45±0.07	11.1±9.3	[VV2000] J230222.5-550827
110	QSO-B1229+204	269.4424	81.7396	0.0637	14.1	0	13.61±0.03	-18.3±3.4	13.63±0.05	-30.5±7.2	Mrk 771
111	SDSSJ092909.79+464424.0	172.5843	46.0101	0.2400	14.1	0	13.28±0.06	-33.1±8.6	13.36±0.08	-6.7±11.0	2MASS J09290979+4644240
112	SDSS-J141309.14+092011.2	354.0972	63.7588	0.4596	14.0	0	13.61±0.03	-2.0±3.2	13.63±0.05	-4.1±5.7	2MASS J14130915+0920109
113	PMNJ2345-1555	65.6728	-70.9851	0.6210	13.7	0	13.62±0.03	-12.2±3.5	13.67±0.05	-14.6±6.1	3FGL J2345.2-1554
114	4C25.01	114.0722	-36.2766	0.2840	13.5	0	13.69±0.03	-15.1±3.0	13.74±0.04	-12.6±5.5	2MASS J00193977+2602522
115	PG0923+201	210.1766	42.6498	0.1922	13.5	0	13.25±0.06	-19.1±8.5	13.29±0.10	-26.9±13.9	Ton 1057
116	HE0435-5304	261.0243	-41.3745	1.2310	13.3	0	13.48±0.04	-3.5±4.3	13.56±0.07	-12.5±8.6	[VV2000] J043650.8-525849
117	QSO-B2356-309	12.8390	-78.0354	0.1654	13.2	0	13.39±0.05	3.9±5.5	13.45±0.08	-5.4±9.7	QSO B2356-309
118	4C-13.41	225.1177	49.1204	0.2410	13.1	0	13.66±0.03	-2.4±3.3	13.67±0.05	8.3±6.2	2XMM J100726.0+124856
119	PG0832+251	199.4909	33.1462	0.3299	12.8	0	13.43±0.04	-13.3±5.4	13.42±0.08	-2.1±9.9	QSO B0832+2510
120	IRAS-F04250-5718	266.9871	-41.9964	0.1040	73.9	1	13.58±0.01	-12.9±0.6	13.67±0.01	-11.3±1.0	LB 1727
121	PKS2005-489	350.3731	-32.6008	0.0710	21.0	1	14.00±0.01	40.1±2.5	14.06±0.02	42.7±2.5	QSO B2005-489
122	PG1211+143	267.5518	74.3150	0.0810	18.6	1	13.58±0.02	-10.8±2.5	13.76±0.03	-4.4±3.0	2E 2620
123	PKS1136-13	277.5252	45.4316	0.5565	18.5	1	13.83±0.02	28.2±2.3	13.93±0.02	29.6±3.0	NAME Crt A
124	PKS0558-504	257.9623	-28.5693	0.1370	18.5	1	13.70±0.02	9.6±2.0	13.81±0.02	7.0±2.9	QSO B0558-5026
125	PG1435-067	343.9784	47.2062	0.1290	18.3	1	13.61±0.02	-36.4±3.3	13.70±0.03	-36.3±4.9	2E 3305
126	2MASS-J14312586+2442203	32.4155	67.4228	0.4070	17.2	1	13.78±0.02	-40.9±3.2	13.87±0.03	-43.8±4.5	2MASS J1431258+244220
127	RBS2005	97.9384	-36.7987	0.1200	16.7	1	13.75±0.02	1.3±1.8	13.88±0.03	1.3±3.0	2MASS J23255424+2153140
128	MRK841	11.2089	54.6320	0.0364	15.8	1	13.88±0.02	-41.2±3.6	14.03±0.03	-42.4±4.0	Mrk 841
129	PDS456	10.3923	11.1632	0.1850	14.2	1	14.00±0.02	-7.5±1.9	14.03±0.03	0.6±2.4	QSO B1725-142
130	RXJ2139.7+0246	58.0875	-35.0060	0.2600	12.5	1	13.75±0.03	4.8±2.9	13.84±0.04	1.9±4.1	2MASS J21394418+0246052
131	3C273	289.9509	64.3600	0.1580	134.4	-1	14.21±0.01	3.0±3.0	13.82±0.00	-19.9±19.9	3C 273
132	PKS0405-123	204.9271	-41.7563	0.5726	77.0	-1	13.46±0.01	-20.3±20.3	13.25±0.02	-14.9±14.9	PKS 0405-123